ELSEVIER

Journal of Structural Geology 26 (2004) 1727–1747

JOURNAL OF STRUCTURAL GEOLOGY

www.elsevier.com/locate/jsg

Permeability scaling properties of fault damage zones in siliclastic rocks

N.E. Odling*, S.D. Harris, R.J. Knipe

Rock Deformation Research Group, School of Earth Sciences, University of Leeds, Leeds LS2 9JT, UK

Received 15 May 2002; received in revised form 17 April 2003; accepted 11 February 2004

Available online 2 April 2004

Abstract

Natural fault damage zones are composed of clusters of sub-seismic-scale faults surrounding larger faults. In siliclastic rocks these faults often form partial barriers to flow and significantly influence fluid flow. A three-dimensional statistical model of fault damage zone architecture, incorporating fault size, orientation and spatial characteristics observed in natural examples, is used with a two-dimensional discrete fault flow model to investigate fluid flow and up-scaling of permeability in fault damage zones with a permeability contrast between rock matrix and fault rock of four orders of magnitude. Models that incorporate realistic fault orientation distributions show mean bulk permeabilities that are up to two orders of magnitude lower than the rock matrix. Incorporating spatial clustering of smaller-scale faults around large faults results in a higher variance of bulk permeability. The degree of 'efficiency' of 50 by 50 m faulted regions (spanning the fault damage zone) is characterized by comparing their bulk permeability with that of the same sized two-dimensional region with a single spanning fault of constant thickness such that the two areas contain the same proportion of fault rock. Regions of size 50 by 50 m are found to be around 50% efficient in the direction perpendicular to the main fault and between 1 and 10% efficient parallel to the main fault. The efficiency of the fault network, thus defined, was found to be insensitive to the exponent of the power law length distribution. This concept of fault damage zone efficiency and the modelling results provide a method of estimating bulk rock permeability from measurements of the fault rock proportion from core or bore-hole logs. Bulk fault zone permeability consists of contributions from the fault damage zone and the fault slip zone on which the majority of the displacement takes place. Estimates of the contribution of the slip zone suggest that the fault damage zone contributes significantly to the bulk permeability of the entire fault zone when slip zone fault rocks have permeabilities no lower than around one order of magnitude less than that of deformation bands. However, even when the slip zone dominates the fault zone bulk permeability, the fault damage zone is likely to have an important influence on flow processes, such as fault seal.

Keywords: Permeability scaling properties; Fault damage zones; Siliclastic rocks

1. Introduction

Predicting the hydraulic behaviour of faults is one of the greatest uncertainties in reservoir- and aquifer-scale flow modelling. Major faults are typically composed of a slip zone, within which most of the displacement occurs, surrounded by a damage zone of minor faults which extends from metres to tens of metres on either side (Chester and Logan, 1986). The damage zone itself can have a major impact on fluid flow and so, when characterizing the impact of the fault, both the major slip zone and the damage zone should be taken into account (Caine and Forster, 1999). The limitations in the resolution of seismic data remain such that, although major faults are detected, there is little or no information on the nature of their damage zones. Thus, one of the main methods of investigating the hydraulic properties of major fault damage zones is through the study of field analogues and the use of flow simulations in which models of the fault damage zone architecture are included explicitly. Due to the limitations on the number of grid cells that can be included in reservoir-scale flow models, major faults are often either represented by zones only one cell thick or incorporated in the properties of the boundary between two cells. In these models, the bulk, or up-scaled, hydraulic properties of the fault and its damage zone are required. Thus, methods are required to accurately determine the bulk properties of major faults and their damage zones from limited in situ data. In this article, the hydraulic properties of major fault damage zones are studied through the stochastic simulation of fault networks and the application of a discrete fracture flow model. Results are

* Corresponding author. Tel.: +44-113-343-5208; fax: +44-113-245-6233.

E-mail address: noelle@rdr.leeds.ac.uk (N.E. Odling).

0191-8141/$ - see front matter © 2004 Elsevier Ltd. All rights reserved.
doi:10.1016/j.jsg.2004.02.005

presented to illustrate the nature of fluid flow through a fault damage zone and the up-scaling of the results in the form of bulk permeability.

2. Fault damage zone characteristics

Large-scale faults are surrounded by clusters of sub-seismic-scale faults that together form a complex deformation volume or damage zone. A number of field studies over the last 10 years have focused on the architecture of fault damage zones in both crystalline and siliclastic sedimentary rocks (Sibson, 1992; Antonellini and Aydin, 1994, 1995; Fowles and Burley, 1994; McGrath and Davidson, 1995; Caine et al., 1996; Knipe et al., 1998; Antonellini et al., 1999; Caine and Forster, 1999; Hesthammer et al., 2000; Flodin et al., 2001; Shipton and Cowie, 2001; Jourde et al., 2002; Shipton et al., 2002). These show that major faults are commonly composed of a major slip zone of one or more major slip surfaces, along which the majority of the displacement occurs, surrounded by a damage zone comprising a complex network of low-throw faults. In siliclastic sedimentary rocks these faults often take the form of deformation bands along which grain size and porosity are reduced to form a partial barrier to fluid flow (Gabrielsen, 1990; Antonellini and Aydin, 1994, 1995; Fowles and Burley, 1994; Fossen and Hesthammer, 1997; Fisher and Knipe, 1998; Caine and Forster, 1999; Aydin, 2000; Hesthammer et al., 2000; Flodin et al., 2001; Shipton and Cowie, 2001; Jourde et al., 2002; Shipton et al., 2002). The connectivity of the sub-seismic fault network within the fault damage zone and the permeability contrast between the rock matrix and deformation bands are major contributors to the effectiveness of the fault zone as a barrier to fluid flow. Deformation bands and slip planes may also be accompanied by open fractures along slip planes and joints that tend to enhance permeability particularly parallel to the major fault plane (Antonellini and Aydin, 1995; Flodin et al., 2001; Jourde et al., 2002). In this article, we focus on fault zones in which minor faults act solely as partial barriers to flow. Such fault zones have been the focus of research in the oil industry for some years. The groundwater community has to date given them less attention, but there is now an increasing realization that such faults can have an important impact on flow direction and contaminant transport in sandstone aquifers (Wealthall et al., 2001).

Detailed studies of fault damage zone architecture around normal faults in siliclastic rocks (Antonellini and Aydin, 1994, 1995; Fowles and Burley, 1994; Foxford et al., 1998; Hesthammer et al., 2000; Shipton and Cowie, 2001; Shipton et al., 2002) have outlined the main characteristics of fault zones (damage zones and fault cores). Generally, the majority of deformation bands and slip planes trend sub-parallel to the major fault with synthetic and antithetic dips (Antonellini and Aydin, 1994; Shipton and Cowie, 2001), although trends highly oblique to the major fault can also occur (Flodin et al., 2001; Jourde et al., 2002). Trends show a scatter of 25–30° about the main fault (Shipton and Cowie, 2001). Synthetic and antithetic structures appear to be coeval and in overall equal proportions for faults with displacement of 30 m and more (Antonellini and Aydin, 1994; Shipton and Cowie, 2001), although the abundance of either set can vary with location within the damage zone (Hesthammer et al., 2000). However, there is considerable scatter in the dips so that the range of dips for each set may overlap (Shipton and Cowie, 2001). Smaller faults with throws of less than 20 m show a dominance of synthetic structures, suggesting that antithetic structures are formed later in the development of the fault in order to accommodate increasing deformation in the rock surrounding the major slip plane (Hesthammer et al., 2000).

Within the damage zone, deformation bands and zones of deformation bands form well-connected systems in 3D with eye and ramp structures on a wide range of scales (Antonellini and Aydin, 1994). Slip planes are less abundant than deformation bands and are segmented and unconnected (Antonellini and Aydin, 1994; Shipton and Cowie, 2001). The width of the damage zone generally correlates with fault throw (Fossen and Hesthammer, 1997; Beach et al., 1999; Shipton and Cowie, 2001) and Beach et al. (1999) found a logarithmic relationship. The damage zone width of around 75 m for a fault with a 30 m throw found by Shipton and Cowie (2001) is in agreement with Beach et al. (1999). The highest density of deformation bands in 1D transects perpendicular to the fault plane occurs close to the fault plane and appears to roughly correlate with the throw on the fault. This density of deformation bands was found to range from 150 to 200 per metre for faults with a 1000 m throw (Antonellini and Aydin, 1994), to be around 40 per metre for faults with a 140 m throw (Knott et al., 1996), and to range from 15 to 20 per metre for faults with throws of 30–40 m (Hesthammer et al., 2000; Shipton and Cowie, 2001).

Although there is presently no data on fault length distributions specifically within fault damage zones, fault size populations are frequently found to be power law with a wide range of exponents (Bonnet et al., 2001). Power law fault throw populations within fault damage zones have been observed (Knott et al., 1996) and, since fault length and throw are generally linearly related (see Cowie et al. (1996) for a review), this suggests that fault length distributions for fault damage zones are also power law. The spatial distribution of the minor faults within the damage zone is one of the more challenging characteristics to quantify. Fault frequency profiles across fault damage zones typically show an overall increase towards the major slip plane (Antonellini and Aydin, 1994; Fowles and Burley, 1994; Knott et al., 1996; Beach et al., 1999; Hesthammer et al., 2000; Shipton et al., 2002). These profiles also show a significant variation in frequency and indicate a degree of clustering of the minor faults within the fault damage zone. Field studies of damage zones note that deformation bands occur singly and in clusters around slip planes and that there

is lateral variability in the number and connectivity of deformation bands (Antonellini and Aydin, 1994; Fowles and Burley, 1994; Beach et al., 1999; Shipton and Cowie, 2001). These features also indicate that deformation bands are typically clustered. In this article, we use a statistical model of a fault damage zone that honours the observed length, throw and orientation distributions and simulates the spatial clustering of minor faults, creating frequency profiles that are similar to those observed in nature.

3. Generating statistical models for fault damage zones

A statistical approach is used to create 3D models of a fault damage zone with a range of different characteristics. This statistical approach is fully described in Harris et al. (1999, 2003) and only a brief description is given here. The principal model variables are the fault size, shape and throw distributions, and orientation and spatial distributions. A series of sections through a 3D view of a simulated fault damage zone is shown in Fig. 1.

Field observations and information from the literature are used to constrain the model variables. Fault length is assumed to follow a power law distribution in which the exponent may be varied. A recent review of scaling in natural fracture systems (Bonnet et al., 2001) shows that power law fracture length distributions from the literature exhibit a wide range of exponents from 0.8 to 3.5. However, after selection according to the quality of the data sets and the analyses, this range was reduced to 1.7–2.75 with a maximum around 2.0 (cumulative frequency distribution exponents). In this study, two exponents, 1.8 and 2.2, are chosen for input to the model to represent the range of most commonly occurring exponents.

Fault trend and dip distributions are each assumed to be normally distributed with mean orientation equal to that of the major fault plane and with a standard deviation of around 10°. This corresponds well to the spread of minor fault strikes of 25–30° reported by Shipton and Cowie (2001). In the model, only one mean dip orientation is included, corresponding to synthetic minor faults. Thus the models best simulate damage zones of faults with around 20–30 m of throw for which the minor fault population is dominated by synthetic faults (Hesthammer et al., 2000). The variations in the strike and dip distributions generate a variation in orientation, as is observed in nature, and allows faults within the simulated damage zone to intersect and form connected networks. Each fault is modelled as an ellipse with a horizontal long axis and an aspect ratio that follows a Gaussian distribution with a mean of 2 and a standard deviation of 0.05. The aspect ratio of 2 is typical of isolated normal faults, whilst restricted faults that interact with other faults show a range from 0.5 to 3.5 (Rippon, 1985; Nicol et al., 1996). The variation in aspect ratio allowed in the model helps to mimic the variation in fault shape generated by interacting faults.

The thickness of fault rock is related to fault length, its displacement and the lithology. A review by Gillespie et al. (1992) indicates that fault displacement:length ratios for high porosity sandstones lie in the range of 1:30–1:500, centring on a ratio of around 1:100. Data from Shipton et al. (2002) give ratios of around 1:10–1:60, which suggests a slightly broader spread than quoted in Gillespie et al. (1992). Manzocchi et al. (1999) gives the ratio between fault rock thickness and fault displacement, for major faults, as 1:66 from field observations, with effective ratios of 1:170 suggested for flow modelling. Since minor faults and deformations bands tend to show rather uniform thickness along their length, a ratio for thickness:displacement of 1:100 has been chosen. Thus, in the model, a linear relationship between fault thickness and long-axis length is used with a thickness:length ratio of $1:10^4$. A simple model for throw distribution over the fault plane is applied in which the thickness is a maximum at the fault centre and decreases linearly in all directions towards the fault tip line. This approximates the distribution of throw seen in isolated faults (Childs et al., 1995). Restricted faults show similar overall patterns, although throw distributions are complicated by interaction with other faults. Including the effects of fault interaction on throw is presently beyond the scope of the model, so a simple model in which the throw, and therefore thickness, distribution over each fault plane resembles that of an isolated fault is adopted.

The model incorporates the possibility of two types of fault spatial distribution. In the simplest model (model 1), fault centres are distributed randomly and the location of each fault centre is independent of every other fault centre. This represents the simplest possible spatial distribution and one that is commonly adopted in fault system models (e.g. Caine and Forster, 1999). This spatial distribution does not, however, reproduce natural fault frequency profiles around a fault, since model frequency profiles across the fault approach a uniform distribution (see Fig. 2a). To provide a better model of the pattern in observed fault frequency distributions, a clustered spatial distribution is generated by concentrating small faults around large faults in a hierarchical fashion. In this model (model 3), the major (longest) fault has the greatest proportion of minor faults around it, but other large faults within the damage zone also have clusters of smaller faults associated with them. Fig. 1 shows an example of a 3D fault damage zone simulation with spatial clustering which clearly demonstrates the hierarchical clustering of small faults around larger ones.

A total of six 3D models of fault damage zones, comprising two exponents of the fault size distribution (1.8 and 2.2) and the three spatial models described above, were generated using the parameters listed in Tables 1 and 2. These models represent increasing complexity in the modelling techniques and an increasing resemblance to natural fault damage zone systems. Model 1 comprises a random fault orientation distribution with a random spatial distribution. This represents the simplest possible damage

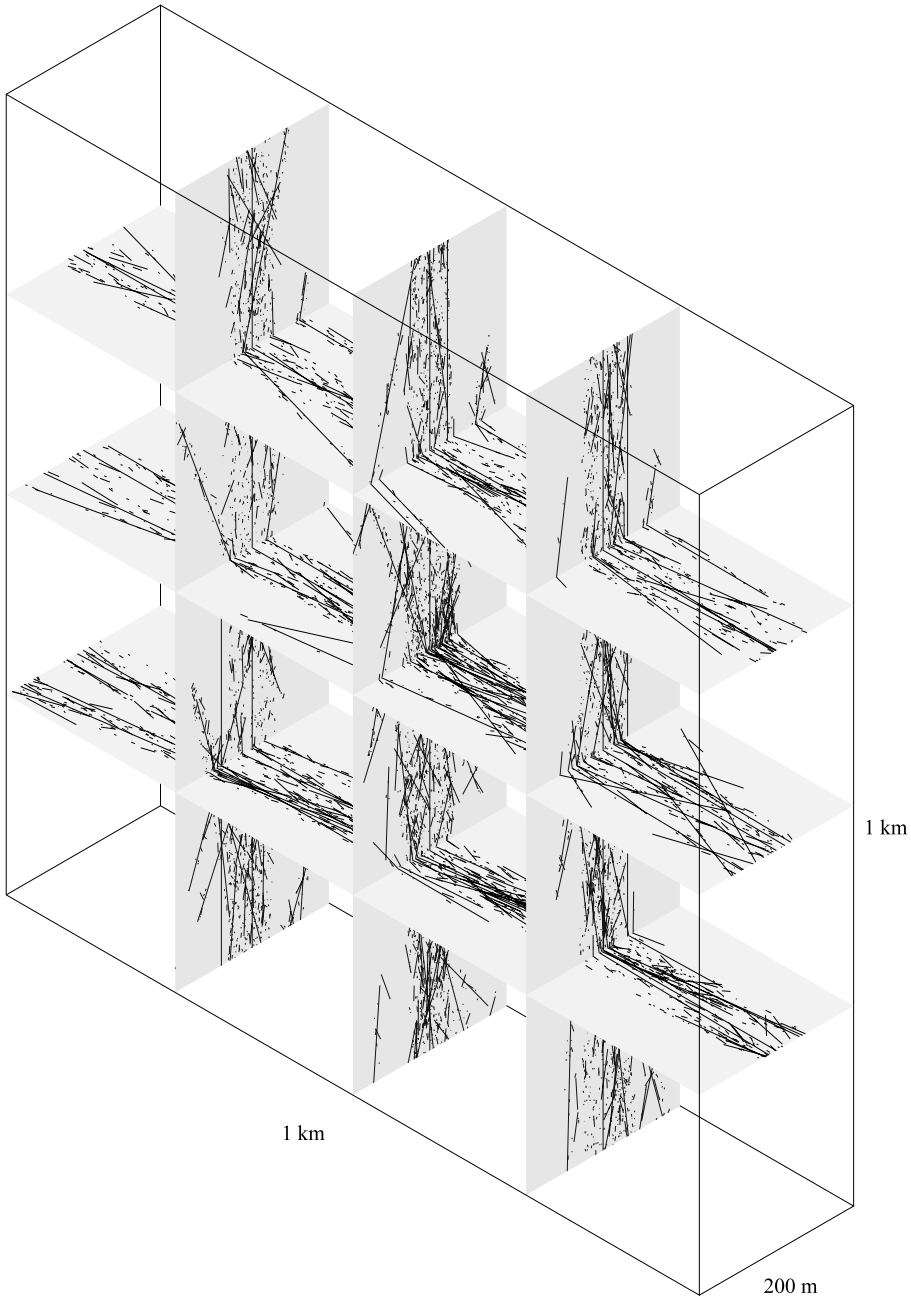

Fig. 1. A view of sections through a 3D stochastic model of a fault damage zone. The fault population has a power law length distribution and small faults are clustered around the larger faults in a hierarchical fashion (model 3).

Table 1
Fault damage zone models: constant input parameters

Fault attributes	Value
Maximum fault length, l_{max} (m)	10,000
Minimum fault length, l_{min} (m)	2.5
Aspect ratio	Gaussian: $\mu = 2$, $\sigma = 0.05$
Fault plunge angle	0°
Fault length:thickness ratio	10,000:1

zone model and provides a base case that allows the impact of more geologically realistic fault orientation and spatial distributions to be quantified. Model 2 includes the fault orientation distribution with a mean parallel to the major fault and a spatially random distribution of fault locations. This corresponds to commonly used models for zones of intense fracturing, including fault damage zones (Caine and Forster, 1999). The final model 3 resembles model 2 but incorporates spatial hierarchical clustering of faults to test the impact of more geologically realistic spatial distributions.

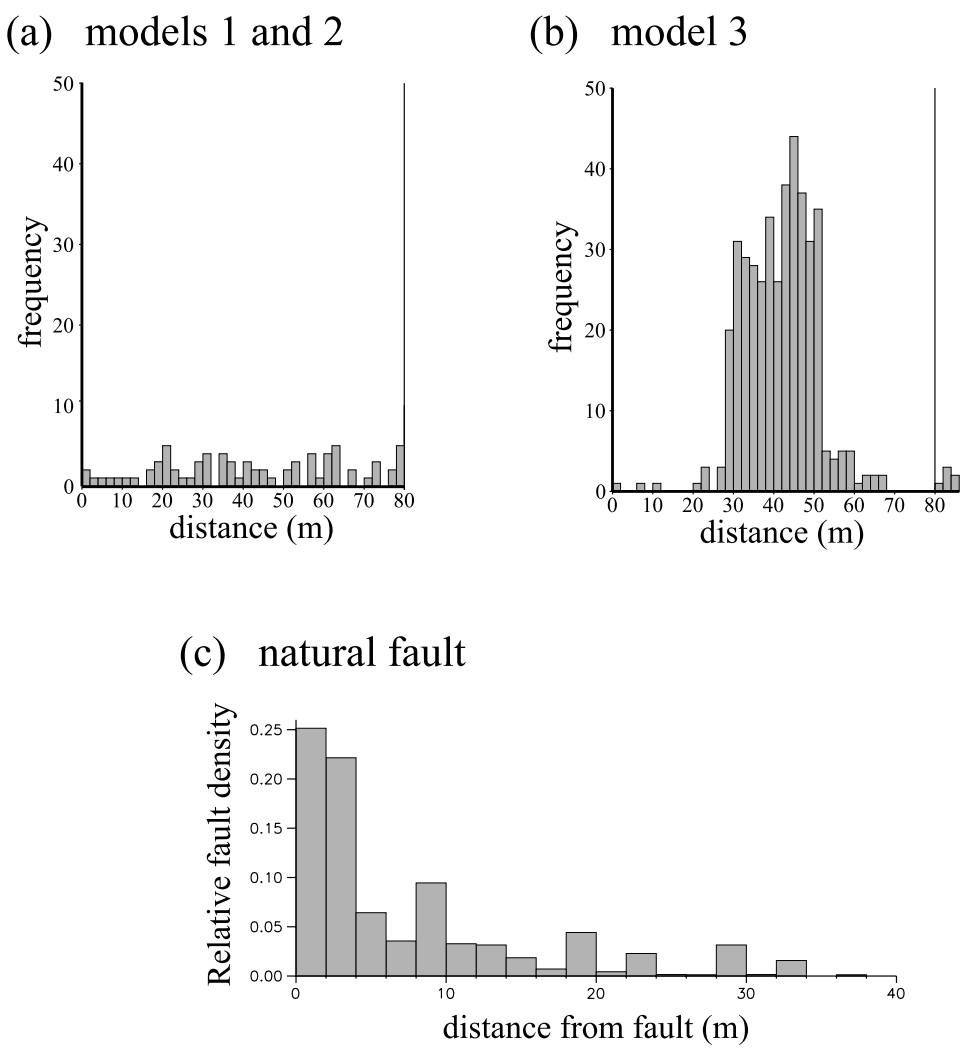

Fig. 2. Fault frequency profiles across the three fault damage zone models: (a) a profile representative of models 1 and 2 (random spatial distributions) which shows a uniform frequency profile, and (b) model 3 (fault trend and clustered spatial distribution) where frequencies increase towards the location of the major fault at 40 m. These model profiles can be compared with the frequency profile across a natural fault (the Ninety Fathom fault, Northumberland, UK) in (c). Model 3 shows a profile type that most closely resembles the natural case.

Each of the 3D models of a fault damage zone represents a cuboidal region centred on the major fault plane (see Fig. 8a). This major fault plane is represented by an ellipse with a horizontal long axis of 3 km and a vertical short axis of 1.5 km. The simulated fault damage zone volume measures 1 km horizontally parallel to the fault trend, 150 m in the vertical direction, and is 80 m thick. For all models this volume contains 1.5 million faults. In Fig. 2, the frequency of faults in 1D transects perpendicular to the main fault are shown and examples of 2D sections through these three models are illustrated in Fig. 3. For the frequency profiles (Fig. 2), models 1 and 2 show an overall constant frequency across the damage zone produced by the random spatial distribution model (Fig. 2a). Model 3, with a hierarchical clustering of faults, produces an overall clustering around the major fault plane (Fig. 2b). This frequency distribution shows the many subordinate peaks within the profile that are observed across natural fault damage zones, an example of which (from the Ninety Fathom fault in Northumberland, England; Harris et al., 2003) is shown in Fig. 2c. Fig. 2c also

Table 2
Fault damage zone models: modified input parameters

Model	Spatial model	Orientation	Length exponents
1	Random	Random dip and strike	1.8, 2.2
2	Random	Gaussian dip and strike, $\sigma = 10°$	1.8, 2.2
3	Hierarchical clustering	Approximately Gaussian, $\sigma > 10°$	1.8, 2.2

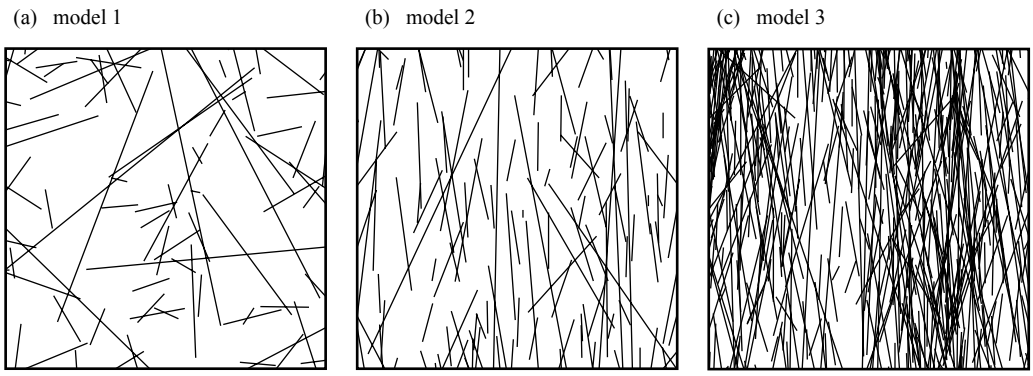

Fig. 3. 2D sections (20 by 20 m) through 3D fault damage zone simulations illustrating the three spatial and orientation models. (a) Model 1: random spatial distribution of fault centres and random orientation distribution. (b) Model 2: random spatial distribution of fault centres with fault orientations normally distributed about the trace of the major fault. (c) Model 3: small faults are clustered around larger faults in a hierarchical fashion and orientations are approximately normally distributed about the major fault trace.

shows that the minor faults are concentrated in a zone about 40–50 m wide and that the maximum frequencies are around 20 per metre. This compares well with the width of fault damage zones and the maximum frequencies of minor faults and deformation bands for normal faults in clean sandstones having lengths of around 3–4 km and with throws of around 30–40 m (Hesthammer et al., 2000; Shipton and Cowie, 2001).

4. Up-scaling of bulk permeability in heterogeneous rocks

Flow modelling is today routinely used to predict hydrocarbon reservoir and aquifer behaviour and to plan hydrocarbon production and water abstraction strategies. The first step in this process is to build a geological model of the reservoir or aquifer, which honours the available data from seismic, bore-hole log and laboratory sources. Gaps in the data can be filled through stochastic modelling of small-scale heterogeneities, such as sedimentary structure and sub-seismic faults. This geological model frequently incorporates heterogeneities on scales of a few centimetres upwards and typically contains of the order of 10^7 grid cells (Pickup et al., 1995). Grid cells are commonly a few tens of metres horizontally and a few metres vertically. Flow simulators, however, are limited to 10^4 to 10^5 grid cells due to computational limitations, with grid cells typically a few hundreds of metres horizontally and a few tens of metres vertically. Thus, flow simulator cells are typically two to three orders of magnitude larger than cells in the geological model. The process of transforming the geological information on a fine grid into hydraulic properties on the coarser flow simulator grid is known as 'up-scaling' and is a topic of intensive research today. The aim of up-scaling is to reproduce the global behaviour of the reservoir while representing the local behaviour as well as possible. There exists a wide range of up-scaling techniques in the literature that vary in accuracy, applicability and speed. There are a number of good reviews of up-scaling techniques in the literature (e.g. Sanchez-Vila et al., 1995; Kumar et al., 1997; Renard and de Marsily, 1997) that outline the different techniques and their advantages and disadvantages, to which the reader is referred for more details. A brief review is given here.

Up-scaling methods can be divided into analytical, stochastic and deterministic methods. Analytical methods include algorithms for determining upper and lower limits to up-scaled permeability or methods for determining a single average permeability. Cardwell and Parsons limits, commonly used in the petroleum industry, involve arithmetic and harmonic means of cell permeabilities in different sequences (Muskat, 1937; Cardwell and Parsons, 1945). These averages are accurate estimations of bulk permeability parallel (arithmetic mean) and perpendicular (harmonic mean) to infinitely continuous parallel strata. These methods have been used to estimate the bulk permeability of faults and their damage zones, both parallel and perpendicular to the fault, by Antonellini and Aydin (1994, 1995) and Shipton et al. (2002), where they incorporate the different permeability properties of deformation bands, zones of deformation bands, slip planes and the fault core. Averaging algorithms include geometric and power averages, derived through stochastic theory. Power averaging techniques have been compared with arithmetic and harmonic mean averages for up-scaling of the permeability of fault zones by Shipton et al. (2002). Stochastic methods assume that the statistical properties of the permeability field are known and are used to derive analytical expressions for the effective permeability, which is defined as the permeability approached as the sample size increases. An example is the effective permeability of an isotropic random field of permeabilities that is given by the geometric mean of individual cell permeabilities (Matheron, 1967). However, these methods can strictly only be applied to a small number of spatial permeability distributions. Many, if not most, geological situations fall outside these cases. Deterministic methods are applicable where the

fine-scale permeability is known (e.g. from a fine-scale geological model) and these include analytical and numerical solutions of the flow field based on Darcy's law, and the applications of percolation theory, effective media theory, stream line methods (for sand–shale mixtures) and renormalization (Renard and de Marsily, 1997).

The most widely applied method that can be used for any heterogeneity field is the solution of the flow field based on Darcy's law. In complex permeability fields, the problem must be solved numerically and codes that are capable of this are now widely available. In applying numerical flow models to determine block permeability, boundary conditions much be chosen. Up-scaled 'block' permeability is not an intrinsic property, but is dependent on boundary conditions and the permeability variations that surround it. Accurately determining these boundary conditions involves running a fine-scale geological model, or large parts of it, in a flow simulator (Almeida et al., 1996), but this tends to be computationally rather intensive. The classical method is to apply no-flow conditions on the boundaries parallel to the flow direction and a constant pressure difference between the other boundaries. This gives the permeability in the direction of flow. This is a local approach in which the block is considered in isolation from its surroundings. This method of up-scaling has been used for faults and fault zones by Caine and Forster (1999) (open fractures), and Flodin et al. (2001) and Jourde et al. (2002) (fractures as both flow barriers and conduits).

In the following, up-scaling of the permeability field is carried out using the classical approach, i.e. a numerical flow model is used to determine the equivalent permeability of the block as a whole in the direction of the applied pressure gradient. This method allows the complexity of the fault network architecture within the fault damage zone to be taken into account.

5. Flow modelling in rocks where faults are flow barriers

A 2D finite-difference discrete fracture flow model (Odling and Webman, 1991) for flow in fractured rocks has been modified to simulate flow in porous rocks with fractures (faults) as flow barriers. In this flow model, both the faults and the rock matrix are discretized onto a regular square grid (Fig. 4). Each element within this grid is assigned a permeability representative of the rock matrix together with any fault rock. Flow in both the rock matrix and the fault rock is assumed to be laminar, which is valid as long as the flow rates are sufficiently small. In this case, Darcy's law applies in the form:

$$Q = -\frac{k}{\mu}\frac{\mathrm{d}P}{\mathrm{d}l} \tag{1}$$

where Q is the magnitude of the Darcy velocity or the fluid flux per unit cross-sectional area, k is the permeability, μ is the dynamic viscosity of the fluid, and dP/d$l$is the local

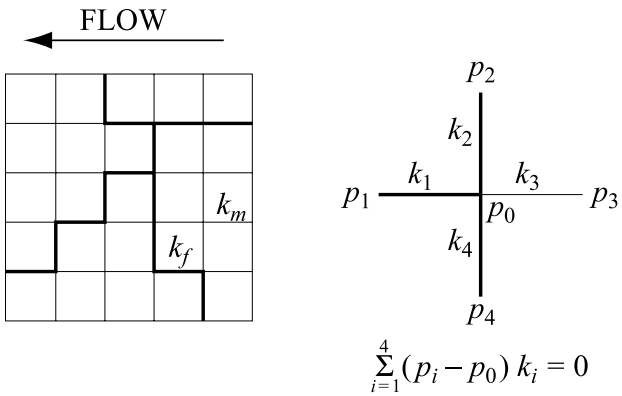

Fig. 4. In the 2D finite-difference flow model, the fault pattern is discretized onto a regular square grid (thick lines) while ensuring that the connectivity properties of the fault system are maintained. The remaining grid elements represent rock matrix. The grid elements are assigned permeabilities representative of faults (k_f) or matrix (k_m). No-flow boundary conditions are applied to the top and bottom of the region and a pressure gradient is imposed from left to right. Darcy's law is assumed to apply (laminar flow) and the pressure field is solved by assuming mass conservation at each node, i.e. that the net flow into each node from the four connecting grid elements equals zero.

pressure gradient. A global pressure gradient is enforced across the model and the pressure at each node is determined by assuming local conservation of flow, i.e. that the net flow towards each node equals zero (see Fig. 4). Having the pressure field, the flow field can be determined using the local permeabilities.

For elements that represent faults, the matrix block represented by a grid element includes a segment of fault (see Fig. 5a). In the case of faults as permeability barriers, a fault can be thought of as a thin plate of low permeability material. The permeability that should be assigned to these blocks in the grid is therefore the bulk permeability associated with the combined matrix and fault. In order to calculate these bulk permeabilities the direction of flow relative to the fault orientation must be identified. The appropriate permeability of blocks representing faults can then be simply calculated using the formulae for adding permeabilities in series and parallel (Muskat, 1937; Pickup et al., 1995) (see Fig. 5b). For flow along a grid element parallel to a fault the arithmetic average of permeabilities is used:

$$\bar{k} = \frac{\sum_{i=1}^{N} t_i k_i}{\sum_{i=1}^{N} t_i} \tag{2}$$

and for flow along a grid element perpendicular to a fault the harmonic average is used:

$$\bar{k} = \left[\frac{\sum_{i=1}^{N} t_i/k_i}{\sum_{i=1}^{N} t_i}\right]^{-1} \tag{3}$$

where t_i is the thickness of each of the N layers and k_i is the corresponding permeability.

Eqs. (2) and (3) are precise for the case when the fault is parallel to the grid directions. However, in the majority of cases the fault is at an angle to the grid directions. To

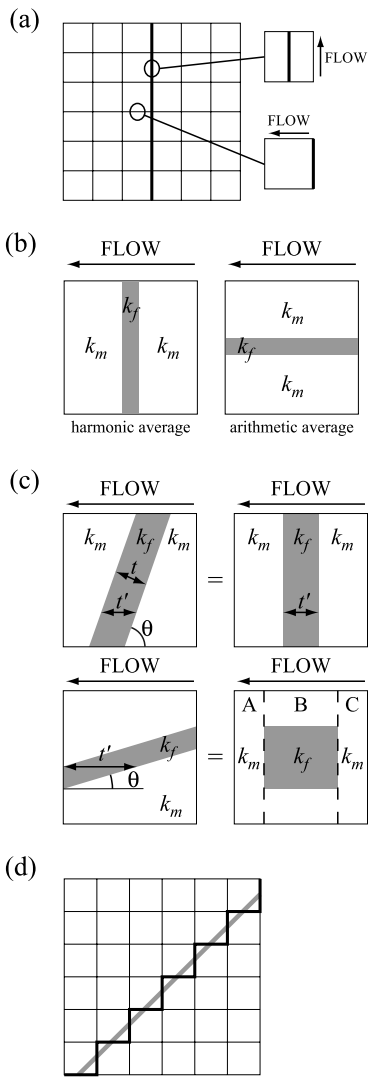

Fig. 5. Discretization of faults onto a regular grid for input to the flow model. (a) In the case of faults as flow barriers, the faults are represented by thin plates of low permeability material. The presence of a fault must be taken into account for grid elements that lie along, or abut against, the discretized trace of the fault. (b) The permeabilities assigned to grid elements are given by the harmonic average of matrix and fault permeabilities when the fault is perpendicular to the flow direction, and by the arithmetic average of these permeabilities when the fault is parallel to the flow direction. (c) In calculating the effective permeability for a grid element, the effective thickness, t', of a fault whose angle, θ, to the flow direction is greater than 45° is used. For faults at angles, θ, less that 45° to the flow direction, the harmonic average permeability of sections A, B and C is calculated, where the permeability of the central section, B, containing the fault is given by the harmonic average of the permeabilities in that section. (d) Where a fault is oblique to the grid directions, it is represented by a staircase geometry. A correction is made to the permeability assigned to fault elements to account for the resulting increase in length.

investigate the effect of orientation, a large-scale flow model was run, in which the layer representing the fault was 10 cells wide in a grid of 100 by 100. It was found that, for layer angles, θ, of greater than 45° to the imposed pressure gradient, the effective thickness, $t' = t/\sin\theta$, of the layer must be used (see Fig. 5c), and the bulk permeability (relative to the matrix permeability k_m) to be assigned to the grid element is:

$$\bar{k} = \left[1 - \frac{t}{\sin\theta} + \frac{t/\sin\theta}{r}\right]^{-1} \tag{4}$$

where r is the ratio of the fault permeability to the matrix permeability. By contrast, for angles $\theta < 45°$ the fault is a discontinuous barrier (see Fig. 5c), and flow can take place through the matrix, around the fault, resulting in a bulk permeability much closer to the matrix permeability. Here, bulk permeability can be closely approximated by summing the permeabilities of sections in parallel (see Fig. 5c), where the permeability of the central section B containing the fault is obtained using the harmonic average of fault and matrix permeabilities. This results in the following formula for the bulk permeability of a grid block:

$$\bar{k} = \left[\frac{t/\sin\theta}{(\tan\theta + t/\cos\theta)/r + 1 - \tan\theta - t/\cos\theta} + 1 - \frac{t}{\sin\theta}\right]^{-1} \tag{5}$$

The two equations (4) and (5) are used to assign permeabilities to grid elements that represent fault elements.

An additional correction must also be made for the effect of gridding on fault length. When a fault is parallel to the directions of the grid, the gridded length is equivalent to the true fault length. However, when the fault is oblique to these directions it is represented by a 'staircase' of grid elements, the summed length of which is greater than the original fault length (see Fig. 5d). To compensate for this, a correction factor is applied that decreases fault element permeability, thus ensuring the correct flow for a given pressure gradient. The correction depends on the angle, θ, of the fault to the grid, and the following three cases arise:

$$k' = \frac{k(\sin\theta - \frac{1}{2}\cos\theta)}{\sin\theta + \cos\theta} \text{ for } \theta \geq 63.4° \tag{6}$$

$$k' = \frac{k}{2} \text{ for } 33.7° \leq \theta \leq 63.4° \tag{7}$$

$$k' = \frac{k(\cos\theta - \frac{1}{2}\sin\theta)}{\sin\theta + \cos\theta} \text{ for } \theta \leq 33.7° \tag{8}$$

In large grids and detailed fault networks it may be possible for the thickness of a fault to exceed the size of a grid element. If this occurs the excess thickness is equally divided between the grid elements on either side.

In discretizing the fault network onto the regular square grid, the connectivity of the network can become altered. The most common effect is that faults may become connected where they were not before. Such effects can seriously affect the flow through the faulted region. Automatic checks are performed against the connectivity of the original fault map to ensure that the connectivity of the gridded networks correctly reflects the connectivity of the system. The above corrections for the grid orientation and the connectivity checks ensure that the characteristics of the fault network that control flow are correctly represented

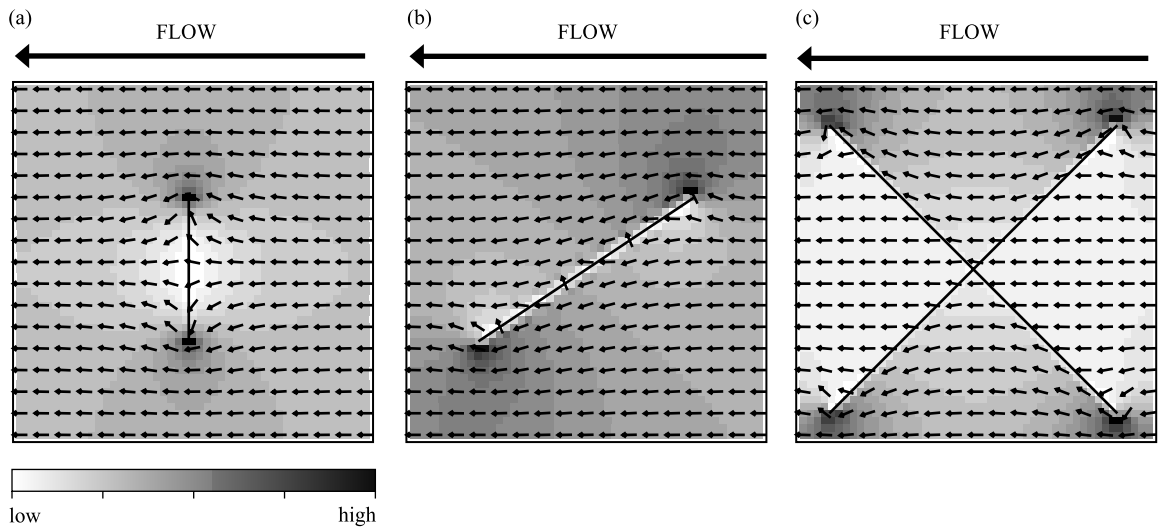

Fig. 6. Flow simulation results for three simple fault geometries using regions of 1 m in size, faults of 5 mm in thickness, and a permeability contrast (matrix/fault rock) of four orders of magnitude. White—low flow speed; black—high flow speed; arrows—flow velocity direction. (a) For a single fault the highest flows occur around the ends of the fault and the lowest flows occur near to the fault centre, since fluid is deflected from the central portions to the fault tips. Some flow through the fault also occurs. (b) In the case of an oblique fault, the highest flows occur near the fault tips and lowest flows on the opposite sides of the fault. The fault causes a deflection in the flow field close to it, but still also allows some fluid to pass through. (c) In the case of two oblique faults, the lowest flows occur in the quadrants open to the inflow and outflow boundaries. In the other quadrants the flow is deflected towards the fault intersection.

in the model and that the model results are independent of the grid size.

Three simple examples are used to show the effect of flow barriers on the flow characteristics (see Fig. 6). Here, flow is simulated in a region 1 m across containing one or two 5-mm-thick faults, with a permeability contrast between rock matrix and fault rock of four orders of magnitude, namely $r = 10^{-4}$. Fig. 6a shows the flow field in a region with a single fault oriented perpendicular to the pressure gradient. The plot shows that flow goes both through and around the fault. The greatest flow rates are generated around the fault tips and the lowest flow is at the fault mid-point. Fig. 6b shows the flow field in a region containing a fault oblique to the pressure gradient. Here, flow is deflected to become nearly parallel to the fault. There is some flow through the fault, but the greatest flows are again around the fault tips. Areas of lowest flow are in the 'shadow' regions close to the fault tips, so that regions of highest and lowest flow rate are juxtaposed across the fault. Fig. 6c shows the flow field in a region containing a symmetrical arrangement of two oblique faults. Here, flow is larger in the top and bottom quadrants defined by the faults and flow paths curve towards the fault intersection. Again, flow is greatest around the fault tips but a significant proportion of the flow crosses the faults themselves. The lowest flow occurs where the faults cross and close to the fault tips, where flow diverges to go either around the fault tips or obliquely across the faults.

Using the flow model, the nature of the flow fields in complex fault networks in permeable rocks can be simulated. The use of large grids, up to 400 by 400 in size, allows the fault networks to be faithfully reproduced in the model. Examples of the flow fields determined by the model for a 2D region, 5 by 5 m in size, from a section through one of the simulations of a fault damage zone, are shown in Fig. 7. The flow field for a pressure gradient imposed perpendicular to the main fault (Fig. 7a) shows small areas of concentrated flow through narrow passages between the faults and at selected points along the faults. The arrows show how flow directions vary through almost 180°. The effect of many faults in the region is to 'compartmentalize' the flow field into regions of higher and lower flow with large contrasts in flow rate across faults. This is especially noticeable where the pressure gradient is placed parallel to the fault trend so that flow becomes concentrated into bands through the fault system (see Fig. 7b).

6. Numerical experiment and scaling of bulk permeability

6.1. 2D sampling of the 3D models for input to the flow model

Within the simulated volume, a total of 13 equally-spaced horizontal 2D sections were chosen (see Fig. 8a and b). In each of these sections, 2D sub-regions ranging in size from 5 to 50 m were sub-sampled to provide input to the flow model. These sub-regions, regardless of size, were centred on points 50 m apart along the trace of the major fault (see Fig. 8c). This ensures that each set of 2D sub-regions samples the whole length of the cross-sections. For each 3D fault damage model, a total of 260 samples (13 sections, 20 sub-regions for each) were taken for each of four sub-region sizes (5, 10, 20 and 50 m). For each sub-sample, the major fault has been omitted so that the effects

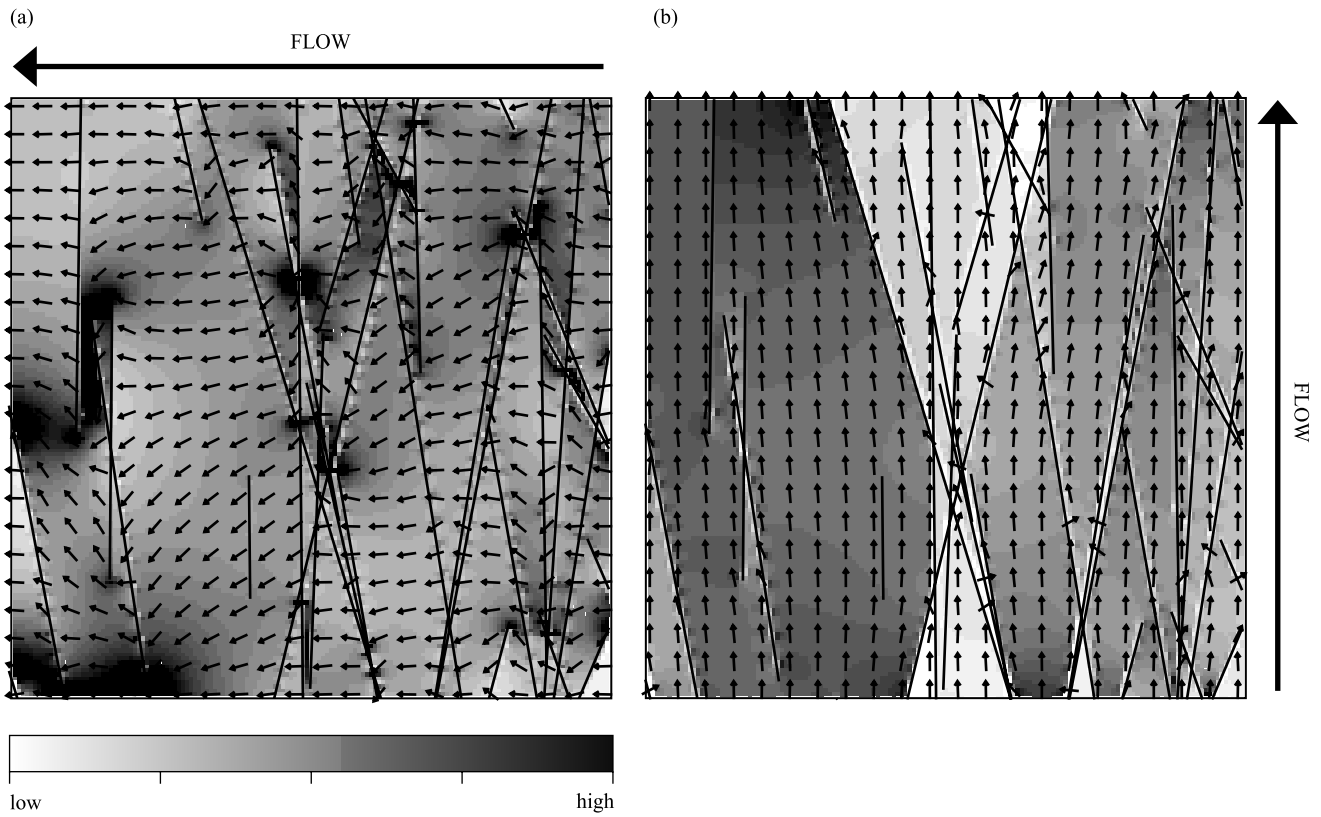

Fig. 7. Examples of the simulated flow fields for a 2D, 5 by 5 m region through the fault damage zone model 3 using a power law exponent of 1.8. White—low flow speed; black—high flow speed; arrows—flow velocity direction. (a) Flow perpendicular to the major fault results in high flow rates through narrow gaps between the faults and where two or more faults intersect. Flow directions range through a wide angle $\pm 90^{\circ}$ from the applied pressure gradient as fluid is deflected around the faults. (b) Flow parallel to the main fault trend results in compartments of high and low flow that are bounded by the larger faults. The range of flow rates is higher (four orders of magnitude) than when flow is perpendicular to the main fault (three orders of magnitude), but flow directions are less variable.

of the fault damage zone alone can be investigated. The major fault plane forms a slip zone of anastomosing faults along which the majority of displacement takes place. The permeability properties of fault rocks formed in this slip zone can be significantly different from those of minor faults in the fault damage zone, so that relationships used in the fault damage zone model may not be appropriate. The potential relative contributions of the slip zone and the fault damage to overall fault bulk permeability are further discussed in Section 9.

6.2. Variations in fault density

Although the 3D fault damage zone models each contain the same number of faults (1.5 million) in the same volume, the fault density in the 2D sections (defined as fault trace length per unit area) varies with the power law length distribution exponent and the type of spatial distribution The examples of 20 by 20 m sub-regions for the three spatial models shown in Fig. 3 illustrate this. The average fault density and its standard deviation for 2D sections through each model are plotted against sub-region size in Fig. 9, where it is observed that models with a length exponent of 1.8 show higher densities. This reflects the greater number of long faults and smaller number of short faults in this model relative to the model with a length exponent of 2.2. For a given length exponent, model 3 shows the highest densities, reflecting the clustering of faults around the major fault plane. The standard deviation of the fault density distribution, in Fig. 9b, is a measure of the variation in fault density in the models. All models show a decrease in standard deviation that flattens with increasing model size, so that the difference between sub-region sizes of 20 and 50 m is negligible. Model 3, regardless of the length exponent, shows the highest standard deviation, implying a broader range of fault densities. This reflects the hierarchical clustering of faults in this model.

7. The scaling of bulk permeability in fault damage zones

The input required by the flow model is the fault geometry, the variation in thickness of each fault, and the permeabilities of fault rock and rock matrix The sub-regions sampled from the 3D fault damage zone models, as described above, provide the fault system geometry and fault rock thickness along the faults. A ratio of rock matrix to fault rock permeability of 10^4, representative of the

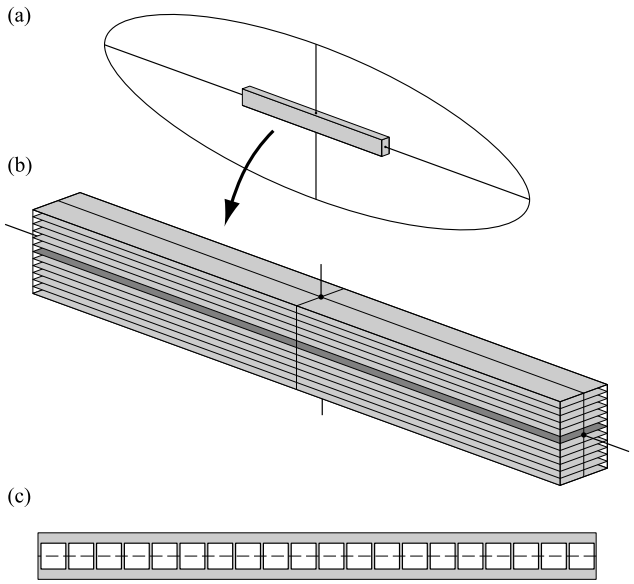

Fig. 8. (a) The relationship between the sample volume and the major fault, which is represented by an ellipse. The main fault is 3 km long (horizontal axis) and 1.5 km wide (vertical axis). The sample volume in which the fault network is simulated measures 1 km horizontally, 150 m vertically and is 80 m wide. (b) The relationship between the sample volume and the sampled 2D sub-regions. The 13 2D horizontal sample planes are shown. (c) An example of a sample plane with the location of the 20 sub-regions, centred at regular intervals along the trace of the main fault.

permeability contrast commonly found between deformation bands and their host rock, is used (Antonellini and Aydin, 1994). The grid size was varied according to the size of the sub-region in order to ensure a valid representation of the fault system geometry. The chosen grids were 150, 200, 300 and 400 for sub-region sizes of 5, 10, 20 and 50 m, respectively. No-flow boundary conditions were applied to the top and bottom of the model and a unit pressure gradient

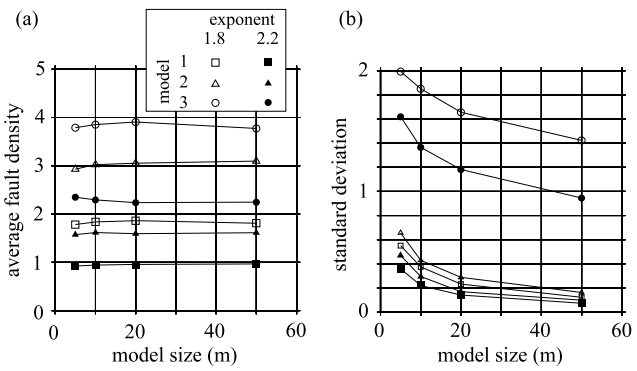

Fig. 9. Variations in (a) the average fault density, defined as the fault trace length per unit area, and (b) the standard deviation, with the sub-region size, calculated from 260 measurements in each case. For a given power law length exponent, model 3 shows the highest fault density and model 1 shows the lowest fault density. In addition, for a given model type, models with a power law exponent of 1.8 show greater fault densities than those with an exponent of 2.2. The range of standard deviations of the fault density distributions shows that model 3 has the greatest variation, while models 1 and 2 show similar, but smaller, variations.

was applied from right to left. The bulk permeability of the sampled region is calculated from the total flux of fluid using Darcy's law. The flow model is applied twice to each sub-region, with the pressure gradient applied perpendicular and parallel to the trend of the major fault.

7.1. The nature of frequency distributions of bulk permeability

The frequency distributions of bulk permeability, determined from the 2D flow simulations in directions perpendicular and parallel to the major fault, have been investigated, and examples are shown in Fig. 10. There are 48 cases (six models, four sub-region sizes and two flow directions), each of which contains 260 values of bulk permeability. The best-fit normal distribution to the log bulk permeability for each case has been determined using the Levenberg–Marquardt method (Press et al., 1992), from which the mean and standard deviation were estimated. The majority of the samples showed acceptable fits to a log–normal distribution using the Kolmogorov–Smirnov test (e.g. Cheeney, 1983), with 38 of a total of 48 samples showing fits to a confidence level of 99%. This shows that, generally, bulk permeability is log–normally distributed. However, cases of smaller sub-regions (5 and 10 m), particularly for flow parallel to the trend of the major fault, show asymmetric distributions of log permeability, some of which showed unacceptable fits to a log–normal distribution (see Fig. 10). These distributions are skewed towards the matrix permeability and show a tendency towards a power law distribution with an exponent (slope of the graph) of around 0.9. Smaller sub-regions contain fewer faults with networks that can be poorly connected. These networks allow flow pathways that cross few faults, especially in the direction parallel to the main fault when fault trend is included in the model (models 2 and 3). This results in bulk permeabilities dominated by the matrix permeability and a skewed frequency distribution. Thus bulk permeability is log–normally distributed provided that the samples contain enough faults to provide connected networks.

7.2. Mean log bulk permeability and its variance

For each of the six models, for directions parallel and perpendicular to the main fault, the means of the log bulk permeability (geometric mean) and their variances are plotted in Fig. 11. Generally, bulk permeabilities are between one and two orders of magnitude lower than the rock matrix perpendicular to the main fault, and up to one and a half orders of magnitude lower parallel to the main fault. Although Fig. 11a shows a slightly decreasing trend, bulk permeability is essentially independent of sub-region size. Model 1 (isotropic), as expected, shows similar permeabilities for directions parallel and perpendicular to the main fault. Models 2 and 3 display very similar bulk

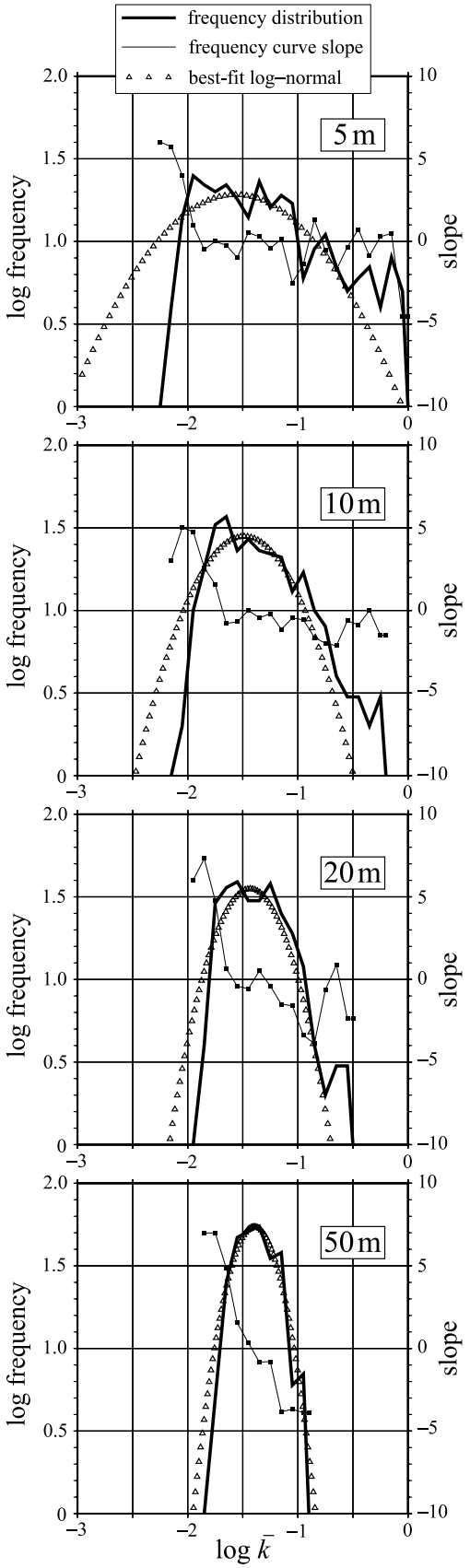

Fig. 10. Examples of frequency distributions of bulk permeability (260 values per distribution) for sub-region sizes of 5, 10, 20 and 50 m for model 3 (clustered spatial distribution with preferential fault trend). Frequency distributions for small sub-region sizes (5 and 10 m) show rather asymmetric shapes, with a tendency towards power law behaviour, while distributions for larger samples show a good fit to a log–normal distribution.

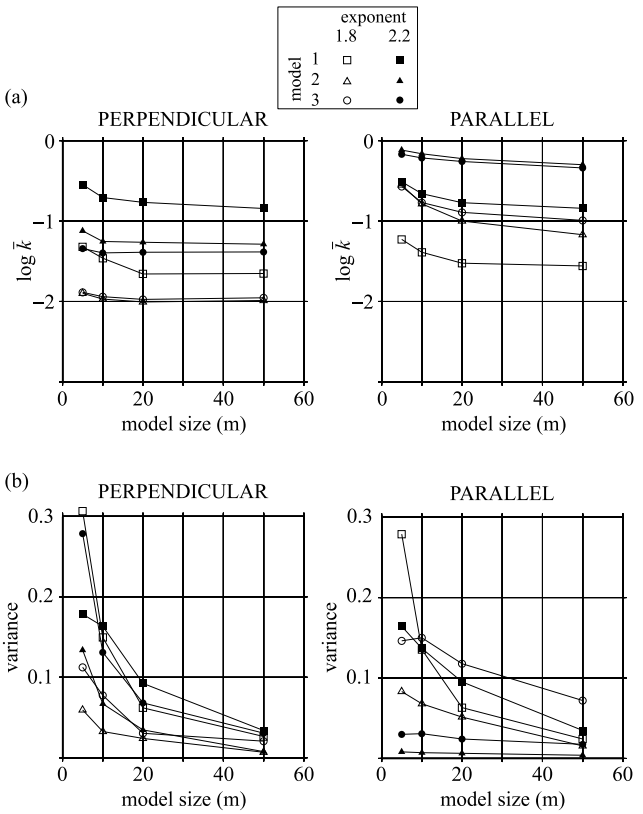

Fig. 11. Variation in (a) bulk permeability and (b) its variance with sub-region size. Bulk permeability perpendicular to the major fault plane is around one order of magnitude lower than that parallel to the main fault plane, except in the case of model 1. Models 2 and 3 with length exponent 1.8 show the lowest permeabilities and are therefore the most efficient barriers to flow across the fault. Most models show a sharp decrease in variance of bulk permeability with increasing sub-region size. The variance has reduced to 0.08, or less, for sub-regions of size 50 m in all models.

permeabilities for a given sub-region size, power law length exponent and direction. They show bulk permeabilities around one half an order of magnitude lower in the direction perpendicular to, and one half of an order of magnitude higher in the direction parallel to the main fault, than model 1. Models with a length exponent of 1.8 show permeabilities around one half of an order of magnitude lower than models with a length exponent of 2.2, for a given sub-region size and direction. This reflects their greater fault trace densities (Fig. 9).

The variances of the bulk permeability distributions characterize the inherent variation in bulk permeability for each model and sub-region size, and are plotted for all

models in Fig. 11b. These plots show a significant decrease in variance of up to around one order of magnitude with increasing sub-region size (5–50 m) for all cases. At a sub-region size of 5 m, the models show a wide range of variances, with model 1 showing the highest and model 2 the lowest variance for a given length exponent and direction. At sub-regions of 50 m, all models show similar variances in the range 0.01–0.07.

As Fig. 11a shows, the introduction of a preferred orientation distribution in models 2 and 3 results in significant permeability anisotropy (maximum:minimum permeability ratio), (see Fig. 12). Model 1, as expected, shows anisotropy ratios close to one. Models 2 and 3 show higher anisotropies in the range 7–23, and decreasing anisotropy with increasing sub-region size. Models with a length exponent of 1.8 show the greatest change with the highest anisotropies (>20) at the small sub-region size and the lowest anisotropies (6–9) at the largest sub-region size.

8. Fault rock proportion and bulk rock permeability

The bulk permeability of a region containing faults is the result of a complex interplay between the fault geometry and fault rock thickness A simple method of estimating bulk permeability is based on summing the fault thicknesses along a line sample through the rock (Antonellini and Aydin, 1994, 1995; Shipton et al., 2002). An estimate of the bulk permeability with respect to matrix, $\bar{k}$, along this line is then simply given by the harmonic average of fault rock and matrix permeabilities (Muskat, 1937; Pickup et al., 1995), weighted by their relative thicknesses along the sample line:

$$\bar{k} = \frac{\bar{k}'}{k_m} = \left[1 - \frac{a}{A} + \frac{a}{Ar}\right]^{-1} \quad (9)$$

where a is the total fault rock thickness, A is the total line length, $\bar{k}'$ is the bulk permeability and r is the ratio of the fault permeability to the matrix permeability. The 2D equivalent of this 1D approach can be thought of as replacing all of the fault rock in an area with a single fault of uniform thickness that spans the region and is oriented perpendicular to flow (see Fig. 13). In this configuration, the fault rock is at its most efficient as a barrier for flow perpendicular to the fault. Eq. (9) overestimates the bulk permeability in this direction as it assumes straight-line flow paths for fluid along the sample line, whereas flow paths are tortuous and strike a balance between the minimum fault rock traversed and the minimum overall path length. However, Eq. (9) provides a method of measuring the 'efficiency' of the fault system in the 2D sub-regions for which bulk permeability has been determined using the flow model. The equivalent single fault system, for which bulk permeability can be simply derived analytically, represents 100% efficiency, and lower levels of efficiency can then be defined by taking smaller proportions of this single fault thickness. The proportion of fault rock can also be determined from line samples such as cores and bore-hole logs, provided that the angle between the sample line and the fault is large enough to give a reasonable sample of the fault damage zone. The proportion of fault rock to rock matrix from core or from good quality optical or acoustic bore-hole logs is information that is fairly readily available from hydrocarbon reservoirs and aquifers (Hesthammer et al., 2000; Shipton et al., 2002) and more easily obtained than the minor fault length distribution.

In the simulated 2D sample regions from the statistical fault damage zone model, the proportion of fault rock has been determined for all samples for which the bulk permeability has been estimated. Manipulating Eq. (9)

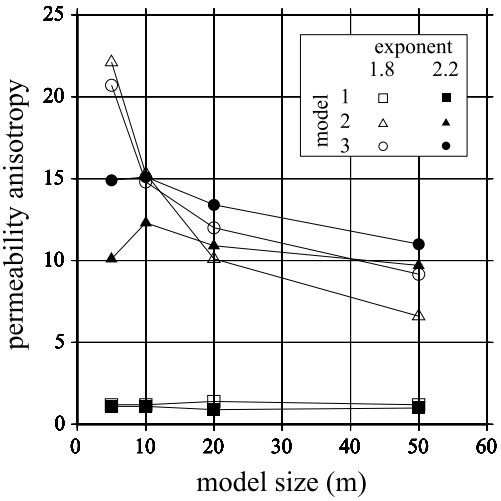

Fig. 12. Mean bulk permeability anisotropy (ratio of bulk permeability perpendicular and parallel to the main fault) versus sub-region size for all models. The degree of anisotropy ranges from 7 to 22, except for model 1 which is isotropic. There is a general decrease in anisotropy with increasing sub-region size. For sub-regions of size 50 m the anisotropy is around one order of magnitude.

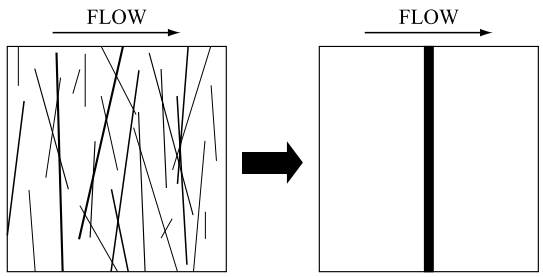

Fig. 13. Definition of fault network efficiency as a barrier to flow. The fault network (left) is replaced by a region of host rock consisting of a single spanning fault of uniform thickness (right). Both regions contain the same proportion of fault rock. The region with a single fault represents the configuration of fault rock that provides the maximum barrier to flow across the region and is defined as being 100% efficient. The bulk permeability of this region can be determined analytically from the harmonic average of host rock and fault rock permeabilities. Lower levels of efficiency are defined by regions with single faults of proportionally lower thickness.

gives:

$$\frac{1}{\bar{k}} - 1 = \frac{a}{A}\left(\frac{1}{r} - 1\right) \quad (10)$$

Thus, in a plot of $\log(1/\bar{k} - 1)$ against the log of the fault rock proportion, a/A, the case of an equivalent single fault that spans the entire region is given by a straight line with a slope of one intercepting the vertical axis (at which $\log(1/\bar{k} - 1) = 0$) at $-\log(1/r - 1)$. Different degrees of efficiency are represented by lines of slope one with different intercepts, so that the $(100\alpha)\%$ efficient line has an intercept of $-\log[\alpha(1/r - 1)]$, where $0 < \alpha < 1$. Such a plot allows easy evaluation of the fault network efficiency for the fault damage zone models. Plots of these quantities for the three models and the four sample region sizes are shown in Fig. 14a and b for power law exponents of 2.2 and 1.8, respectively.

In Fig. 14a and b, the bulk permeability perpendicular and parallel to the main fault are plotted together, for models with length exponents of 1.8 and 2.2. As expected, model 1 (random spatial distribution and orientations) shows a single cloud as bulk permeability is not sensitive to the flow direction. For the other models (2 and 3), bulk permeabilities perpendicular and parallel to the main fault are separated by a little over an order of magnitude in all cases, the bulk permeability parallel to the main fault being the larger and corresponding to lower values of $1/\bar{k} - 1$. As the sample size increases from 5 to 50 m, the spread of both the fault rock proportion and the bulk permeability decreases from around two orders of magnitude to a minimum of half an order of magnitude. Model 2 (random spatial distribution with trend) shows the most tightly clustered distributions, with model 1 (random spatial and orientation distributions) showing the greatest scatter and model 3 (clustered spatial distribution with trend) lying in-between.

Fig. 14a and b shows that the smallest sub-region size (5 m) for all three models has the greatest scatter, ranging from 100 to 10% efficient for bulk permeability perpendicular to the main fault, and from 10% to less than 1% efficient for bulk permeability parallel to the main fault. It is possible for the smallest sub-regions (5 m) to be 100% efficient if they contain faults that span the region perpendicular to the flow direction. Larger sub-regions contain many faults and their efficiency depends on the connectivity of the fault network. Parts of faults that end within the matrix do not act as efficient barriers, and so larger samples always show efficiencies less than 100%. As the sub-region size increases to 50 m, the scatter of the bulk permeabilities for models 2 and 3 cluster close to the 50% efficiency contour for bulk permeability perpendicular to the main fault, and between the 10 and 1% efficiency contours for bulk permeability parallel to the main fault. Generally, the clouds of points for the case of a power law length exponent of 1.8 in Fig. 14b show permeabilities around one order of magnitude lower, and fault rock proportions around a half to one order of magnitude larger, than for the case of a length exponent of 2.2 (Fig. 14a). This reflects the larger proportion of long faults with thicker fault rock in the fault population with a length exponent of 1.8.

Fig. 15 shows a plot of the fault rock proportion versus $1/\bar{k} - 1$ for the case of model 3 (clustered with trend) using the two length exponents 1.8 and 2.2, and a 50 m sub-region size. The bulk permeabilities perpendicular to the main fault for each length exponent form elongate trends arranged en échelon close to the 50% efficiency line. These trends are aligned slightly obliquely to the 50% efficiency line (slope of one) and show a slope of 1.2 over almost an order of magnitude in both cases, with correlation coefficients of 0.97 (linear regression). This suggests that the bulk permeability perpendicular to the main fault, at a scale that encompasses most of the damage zone thickness (50 m), shows a power law relationship with the proportion of fault rock. The exponent of this power law (1.2) shows that bulk permeability decreases more slowly than fault rock thickness increases. Thus, as the fault rock proportion increases due to increasing fault density, there is a slight decrease in the efficiency of the fault system as a flow barrier. For permeability parallel to the main fault, the case of a length exponent of 1.8 shows a slightly higher efficiency than for the case of the exponent 2.2. This is due to the presence of more long faults and their intersections with other faults that make the existence of flow pathways through the matrix less probable for flow in this direction. However, the two trends for exponents 1.8 and 2.2 are very close, and are separated by only a fifth of an order of magnitude in the case of permeability perpendicular to the main fault. This indicates that the efficiency of the system is, in fact, not very sensitive to the power law length exponent, at least within the range 1.8–2.2.

9. Permeability contributions of fault damage zone versus fault slip zone

The analysis of the previous sections concerns the effects of the fault damage zone alone on flow and bulk permeability. However, major fault zones are composed of a slip zone, on which the majority of the displacement takes place, surrounded by the fault damage zone. Slip zones consist of a number of slip surfaces, with an anastamosing geometry, along which cataclasis and mineral precipitation are common (Caine et al., 1996; Knipe et al., 1997, 1998; Shipton and Cowie, 2001; Shipton et al., 2002). Open fractures can also exist within slip zones and thus form potential flow conduits (Caine and Forster, 1999; Flodin et al., 2001; Jourde et al., 2002). The permeabilities of slip zones can therefore be highly anisotropic. The permeability perpendicular to a slip zone dominated by fault rock can show a wide range, down to very low values (Antonellini and Aydin, 1994; Fisher and Knipe, 1998, 2001), and the slip zone can form a significant barrier to flow in its own

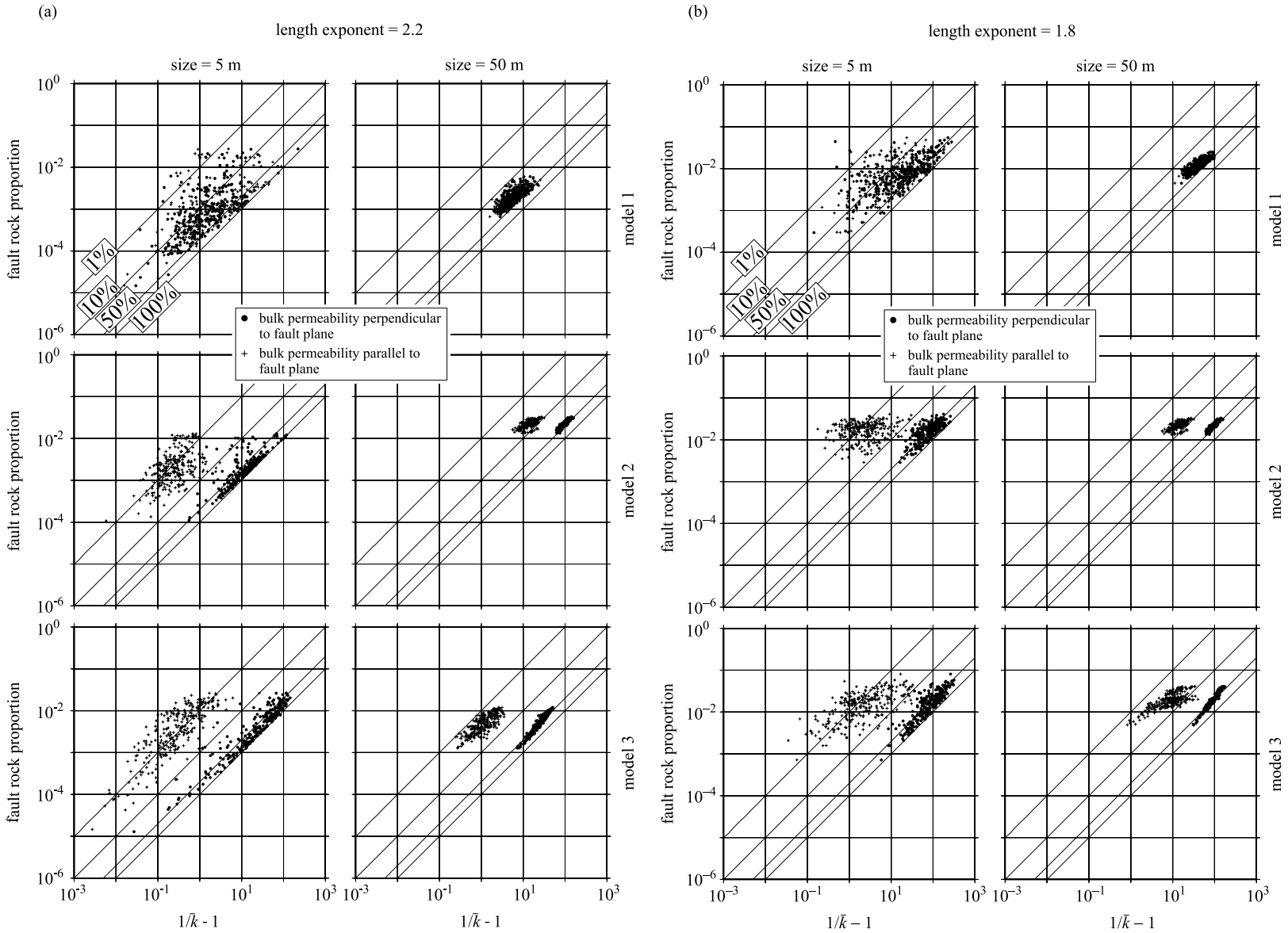

Fig. 14. (a) Log–log plots of fault rock proportion versus $1/\bar{k} - 1$ for all models with power law length exponent 2.2 and sub-region sizes (top to bottom) of 5, 10, 20 and 50 m. Model 1—random spatial and orientation distributions; model 2—random spatial distributions with preferred fault trend; model 3—clustered spatial distribution with preferred fault trend. Bulk permeability values are compared with contours of fault network efficiency (see text and Fig. 13 for detailed definition). For model 1, bulk permeability values for flow perpendicular and parallel to the main fault plane are indistinguishable. Models 2 and 3 are around 50% efficient perpendicular to the main fault and between 1 and 10% efficient parallel to the main fault. The scatter in the bulk permeabilities reduces as the sub-region size decreases. (b) As for (a) but for exponent 1.8. The spread of bulk permeabilities for a given sub-region size is lower than for models with an exponent of 2.2, particularly at smaller sub-region sizes.

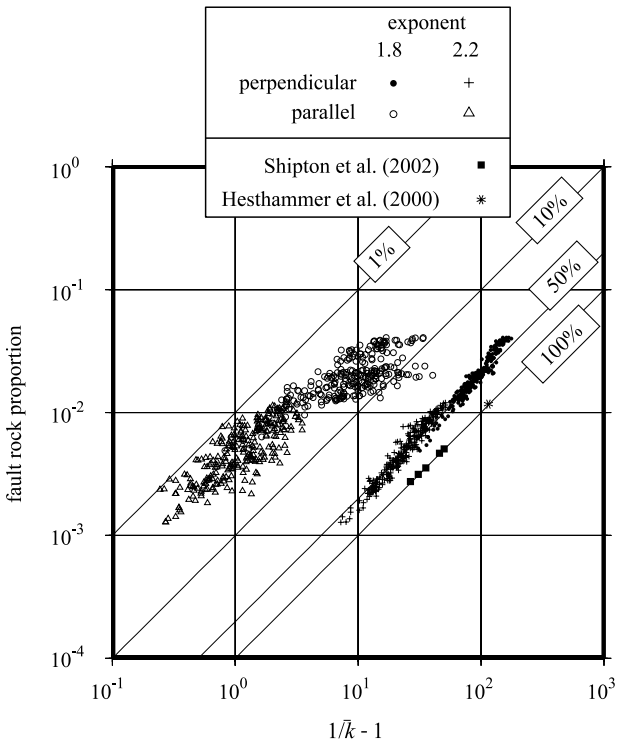

Fig. 15. Log–log plot of fault rock proportion versus $1/\bar{k} - 1$ for sub-region sizes of 50 m for model 3 (clustered spatial distribution and preferred fault trend), showing a comparison of the models for power law length exponents of 1.8 and 2.2. Bulk permeability values perpendicular to the main fault follow en échelon trends that are close to the 50% efficiency line. This shows that the relationship between bulk permeability and fault rock proportion is not very sensitive to the exponent of the power law length distribution.

right. It is of interest to consider the possible range in relative contributions of the fault damage zone and the slip zone to the permeability of the major fault as a whole. Here only the impact of fault rock itself is considered, neglecting any open fracture surfaces associated with the slip zones. The effective permeability of a slip zone depends on both the width of the fault rock material and its permeability. The width of the fault rock is in general related to the amount of displacement on the fault, which in turn is dependent on the size of the fault, the host rock lithologies, rock strengths, and interaction with other faults.

A review of the relationship between fault dimensions and displacement has been made by Gillespie et al. (1992), who summarises a number of large data sets with fault lengths spanning a total range of seven orders of magnitude. The present analysis is based on an isolated fault of 3 km in length (horizontal dimension) in clean, high porosity sandstones. From Gillespie et al. (1992), the data sets from high porosity sandstones indicate that, for a fault with a length, L, of 3 km, possible displacements, D, range from 3 to 100 m, with most faults showing displacements lying in the range of 5–50 m, corresponding to L/D ratios between 60 and 600. Manzocchi et al. (1999) have reviewed the relationship between fault displacement and the cumulative thickness of the fault rock in the fault zone. They show that, on average, the fault rock thickness, t (m), on a slip zone is related to the displacement, D (m), through the following linear relation:

$$t = \frac{D}{66} \tag{11}$$

This is in reasonable agreement with recent data from Shipton and Cowie (2001) for a normal fault in porous sandstones from Utah with a throw of 30 m and a fault core thickness of 30 cm. Eq. (11) would predict a thickness of 45 cm here, which is close to the observed value. However, observations show a wide scatter in which the thickness values for a specific displacement span two orders of magnitude (Evans, 1990; Gillespie et al., 1992; Knott et al., 1996). Observations of outcrops also show that fault zone thickness is highly variable on scales of tens of metres or less within a single fault (Evans, 1990; Shipton and Cowie, 2001; Jourde et al., 2002). In such a geometry, fluid flow across slip zones will tend to concentrate in areas with low net fault rock thickness. Manzocchi et al. (1999) therefore suggest that, over sufficiently large volumes (with dimensions of some tens of metres), the effective thickness of the fault for flow is given by the harmonic average of the thickness data, giving the modified relation:

$$t = \frac{D}{170} \tag{12}$$

The permeability of fault rock material in slip zones ranges widely through several orders of magnitude and depends on the pressure–temperature conditions at the time of fault movement, and the lithology (in particular, the amount of clay minerals present). Studies of fault rocks in high porosity sandstones (Antonellini and Aydin, 1994, 1995; Fisher and Knipe, 1998, 2001) show that their permeability ranges from values similar to that of a deformation band to at least three orders of magnitude lower, a range equivalent to between three and seven orders of magnitude lower than the host rock permeability.

To assess the potential effects of the slip zone relative to the fault damage zone on total fault zone bulk permeability, the bulk permeability of a 50 by 50 m region, spanning the width of the fault damage zone and containing a slip zone, is estimated. Here, it is assumed that the slip zone traverses the whole of the 50 m region, so that the bulk permeability perpendicular to the fault zone is given analytically by the harmonic average of the bulk fault damage zone permeability and the slip zone fault rock permeability:

$$\bar{k}_{\mathrm{tf}} = \left[\frac{1 - t/50}{k_{\mathrm{fdz}}} + \frac{t/50}{k_{\mathrm{sz}}} \right]^{-1} \tag{13}$$

where $\bar{k}_{\mathrm{tf}}$ is the total fault zone bulk permeability, t is the thickness of the fault rock in the major slip zone, k_{fdz} is the bulk permeability of the fault damage zone, and k_{sz} is the permeability of the slip zone fault rock. Here, all

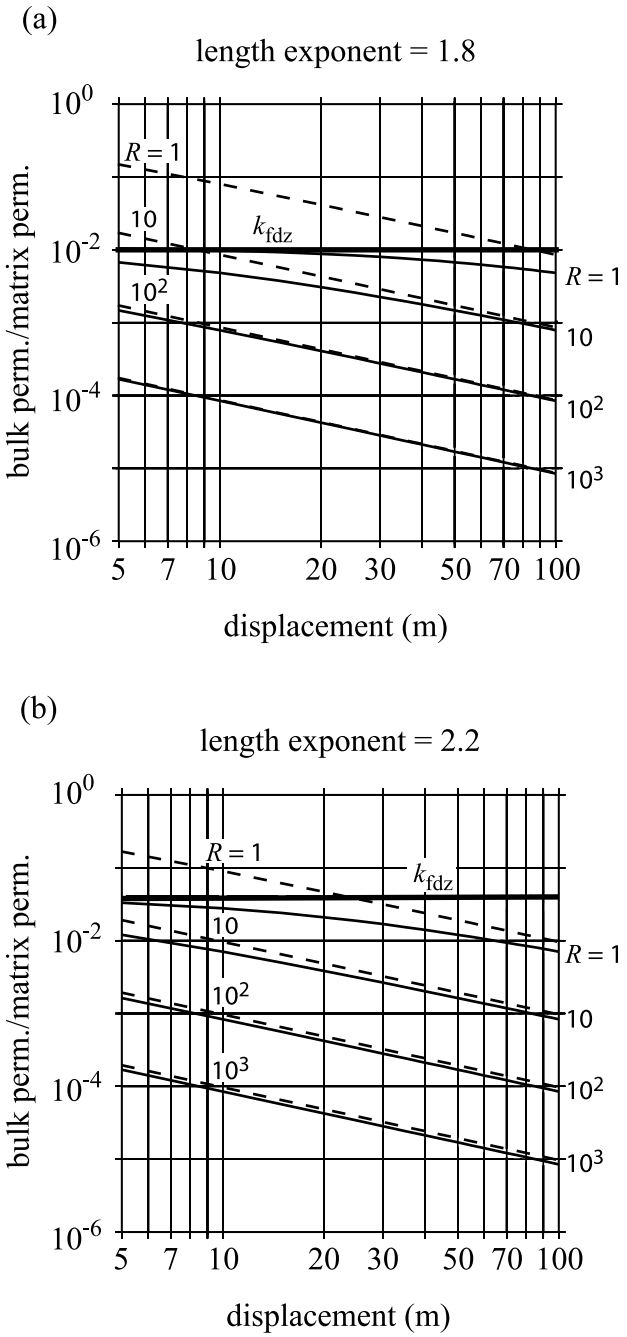

Fig. 16. Relationship between displacement and total fault zone permeability (fault damage zone and slip zone) for model 3 of the fault damage zone using power law fault length exponents of (a) 1.8 and (b) 2.2. In each case, the geometric mean of permeability values determined for the fault damage zone alone is shown by the thick lines (k_{fdz}). The solid thin lines (labels on right) show the permeability of the whole fault zone (fault damage zone and slip zone) for different ratios, R, of the minor fault rock permeability to the slip zone fault rock permeability. The dashed lines (labels on left) show the equivalent contours for the fault slip zone alone. The plots show that the fault damage zone makes a significant contribution to the permeability of the fault zone as a whole when R is less than an order of magnitude.

permeabilities are normalized with respect to the host rock permeability.

The two values of 0.01 and 0.04 (with respect to host rock permeability) for the bulk fault damage zone permeability are used, representing the geometrical means of bulk permeability perpendicular to the major fault for model 3 with fault length distribution exponents of 1.8 and 2.2, respectively. A range of fault displacements ranging from 5 to 100 m is used to calculate the effective fault rock thickness within the major slip zone, using Eq. (12), and this fault rock is assigned a range of permeabilities from four to seven orders of magnitude lower than the host rock (up to three orders of magnitude lower than deformation band permeability). Bulk permeabilities for the fault zone as a whole are then calculated using Eq. (13) and shown as solid lines on a plot of fault displacement versus bulk permeability in Fig. 16. In addition, the impact of the major slip zone alone is calculated for comparison using the host rock permeability in place of the fault damage zone permeability in Eq. (13), and this is shown as dashed lines in Fig. 16. By comparing these two sets of lines, the influence of the damage zone and the slip zone on bulk permeability can be seen.

Fig. 16 shows that the influence of the slip zone itself on the total fault zone bulk permeability increases with increasing displacement in a non-linear fashion. When the major slip zone fault rock has a permeability similar to that of deformation bands ($R = 1$ in Fig. 16), the fault damage zone makes a significant contribution to the bulk permeability (the solid line lies significantly below the dashed line in Fig. 16). However, when the permeability of the slip zone fault rock is an order of magnitude ($R = 10$ in Fig. 16) or more lower than the permeability of deformation bands, the major slip zone dominates the bulk permeability of the whole fault zone (the solid and dashed lines in Fig. 16 are close). These effects are most marked when the fault displacement, and therefore fault rock thickness, is large. Thus, the fault damage zone can be expected to make a significant contribution to the bulk permeability of the whole fault zone in cases where the permeability of the slip zone fault rocks is similar to, or at most one order of magnitude lower than, that of deformation bands. Otherwise, the slip zone dominates the total fault zone bulk permeability.

10. Discussion

A series of stochastically generated 3D models of fault networks in fault damage zones within highly porous sandstones has been generated. The three types of spatial and orientation distribution models represent an increasingly good approximation to the geometry of natural fault damage zones. 2D samples from these models have been used as input to a 2D finite-difference discrete fracture flow model in which the minor faults are modelled with a

permeability four orders of magnitude lower than the host rock, typical of deformation bands in high porosity sandstones. The flow model has then been used to investigate the bulk permeability of faulted rock volumes and its relationship to region size, spatial model, and power law fault length exponent.

The spatial model 3 incorporates hierarchical clustering of faults, and generates fault frequency profiles that closely resemble those observed across natural fault damage zones. The model assumes a single distribution of synthetic fault dips rather than a distribution with two dip modes representing synthetic and antithetic faults. For faults with throws larger than around 20–30 m, damage zones contain both synthetic and antithetic faults (Antonellini and Aydin, 1994; Hesthammer et al., 2000; Shipton and Cowie, 2001), so that our model, which is based on a fault of 3 km length and throw around 30 m, is most representative of smaller-scale faults with throws of 30 m or less. The presence of both synthetic and antithetic faults in the damage zones of larger-scale faults will have an important impact on the 3D connectivity of the system (Antonellini and Aydin, 1994). However, as input to the flow model we have used 2D samples that are perpendicular to the fault plane and contain the direction of the fault long axis. For a normal fault, this sample plane orientation contains the strike direction of the faults, and thus the dip model has no impact on connectivity within this plane. The results we have shown can therefore also be relevant to the bulk permeability within this sample plane, for larger-scale faults. However, if bulk permeability parallel to the major fault short axis (slip direction) is to be determined, it is necessary to include both synthetic and antithetic faults in the model.

In the model we have assumed that all minor faults have a permeability representative of deformation bands. Field observations (Antonellini and Aydin, 1994; Shipton and Cowie, 2001) indicate that slip planes also occur within the damage zone and can have wall rocks of very low permeability. However, these are generally sparse and unconnected within fault damage zones, and only form connected networks in the fault slip zone. Within the damage zone, flow pathways around such slip planes will exist and they will therefore have a minimal effect on the bulk permeability, although their presence will tend to locally increase flow pathway tortuosity.

The simulated flow fields show how the complex fault systems within fault damage zones influence fluid flow. Flow rates span a range of three to four orders of magnitude and are highest around the tips of faults, in narrow gaps between unconnected faults, and at fault intersections. When the applied pressure gradient is parallel to the main fault, the fault system compartmentalizes the region into bands of high and low flow that tend to be delineated by the larger faults. These features show how preferential flow pathways both perpendicular and parallel to the major fault system within the fault damage zones develop. In two-phase flow, the pathways of least flow resistance may transmit hydrocarbons across the fault at lower differential pressures than suggested by the bulk permeability behaviour of the fault. This suggests that faults may leak over a much wider range of pressure conditions than generally assumed.

The bulk permeabilities of fault damage zones determined by the flow model over a range of sub-region sizes show the impact of the different spatial and orientation models. The inclusion of a realistic orientation distribution (models 2 and 3) results in a permeability anisotropy of around an order of magnitude, with permeabilities half an order less than and greater than those of the simple random model (model 1). The addition of hierarchical clustering (model 3) increases the variance in bulk permeability, reflecting a wider range of flow behaviour and suggesting effective sealing over a reduced range of pressure conditions. In the case of a contaminated aquifer, this increased variance suggests greater transport of contaminants across the fault.

Mean bulk permeability does not vary much with sub-region size (5–50 m) but the variance decreases dramatically as the sub-region size increases. In reservoir-scale flow models, grid blocks are around 100 m, large enough to contain the bulk of the damage zone width of many seismically resolvable faults. Such flow models require permeabilities that are representative of the fault damage zone as a whole. The modelling results suggest that these bulk permeabilities are log–normally distributed, with 99% of the distribution lying within one order of magnitude. This distribution of permeability should be used to assign permeabilities to grid blocks in large-scale flow models. In addition, in more detailed flow models with smaller grid blocks, a permeability distribution with a larger variance should be used. This is at odds with the common practice of assigning constant or smoothly varying hydraulic properties along the length of major faults in reservoir-scale flow models, a practice that results largely from a lack of more detailed information. Assigning variable bulk permeabilities along the length of a major fault will concentrate flow through the higher permeability sections of the fault and impact on the sealing properties of the model fault.

The ‘efficiency’ of a faulted region within a fault damage zone as a barrier to flow has been defined with respect to the same sized region with a single fault of uniform thickness, containing the same proportion of fault rock area. The model results indicate that 50 m sub-regions that span the fault damage zone are close to 50% efficient perpendicular to the main fault, but only 1–10% efficient parallel to the main fault. The two power law fault length exponents, 1.8 and 2.2, for model 3 (the most realistic spatial and orientation model) result in two elongate trends on the plot of fault rock proportion versus $1/\bar{k} - 1$.

These trends have a slope of 1.2, slightly oblique to the efficiency contours. Model 3 with a power law length distribution exponent of 1.8 results in permeabilities that are half an order of magnitude lower than those with an exponent of 2.2. Although the models contain the same

number of faults, the greater abundance of longer, and therefore thicker, faults in the model with a length exponent of 1.8 creates a more efficient barrier to flow. However, the two trends are arranged en échelon close to the 50% efficiency line on the plot (Fig. 15) in both cases, differing by only 10–20% for a given fault rock proportion. Thus, the relationship between fault rock proportion and bulk rock permeability is not very sensitive to the length exponent, at least between the exponent values of 1.8 and 2.2. This suggests that the proportion of fault rock as measured along a line sample, for example along a core or bore-hole log, can be used to estimate the bulk rock permeability of the fault damage zones by assuming an efficiency of 50%, regardless of the length distribution of faults. For this estimate the required information is simply the fault rock proportion measured from core or bore-hole logs and laboratory measurements of host rock and fault rock permeability.

Estimates of bulk permeability of normal fault zones in high porosity sandstones, including their damage zones have been made by Antonellini and Aydin (1994, 1995) and Shipton et al. (2002). They used the harmonic average of the permeability of fault components (deformation bands, zones of deformation bands, slip planes and fault core) to estimate the bulk permeability perpendicular to the fault plane, and the arithmetic average for bulk permeability parallel to the fault plane. Antonellini and Aydin (1994) found a reduction of bulk permeability across the fault zone, relative to host rock, of almost two orders of magnitude (1.35×10^{-2}) for a major normal fault with throw in excess of 1000 m. The reduction due to deformation bands alone was closer to one order of magnitude (7×10^{-2}). The ratio of deformation band permeability to host rock permeability in their calculations is 5×10^{-3}. Shipton et al. (2002), using a permeability ratio of deformation band to host rock of 7×10^{-4}, estimated the reduction of bulk permeability, relative to host rock, across normal faults with throws of around 30 m as being up to two orders of magnitude (10^{-2}–3×10^{-2}). These estimates assume infinitely continuous faults, and thus give a lower limit to bulk permeability perpendicular to, and an upper limit on bulk permeability parallel to, the major fault.

To compare the above estimates of bulk permeability with those from the modelling presented here, the data on fault damage zone width, number of deformation bands and deformation band width from Shipton et al. (2002, Table 4) was used to recalculate bulk permeability perpendicular to the major fault from deformation bands alone, assuming a permeability ratio between deformation bands and host rock of 10^{-4}. This exercise has also been applied to data from Hesthammer et al. (2000) from a frequency histogram of deformation bands in a fault damage zone from a 45 m throw normal fault in the Gulfaks field. Here a deformation bandwidth of 1 mm, as in Shipton et al. (2002), which lies within their observed range (0.5–5 mm), is assumed. This gave bulk permeabilities relative to host rock across the fault zones ranging from 2×10^{-2} to 3.6×10^{-2} for the data from Shipton et al. (2002) and 9×10^{-3} for the data of Hesthammer et al. (2000). Converting these values to $1/\bar{k} - 1$ and calculating the total deformation band width as a proportion of the damage zone width (fault rock proportion) allows these values to be plotted on Fig. 15 and compared with the model results. Since the harmonic average was used to calculate these bulk permeabilities, they plot on the 100% efficiency line (see Fig.15). At the corresponding 50% efficiency, the data from Shipton et al. (2002) plot near the centre of results from model 3 with a length exponent of 2.2, while the data from Hesthammer et al. (2000) plot near the centre of results from model 3 with a length exponent of 1.8, and thus both agree well with the model results.

For an estimate of bulk permeability parallel to the major fault, Antonellini and Aydin (1994) and Shipton et al. (2002) used the arithmetic average of permeabilities of fault zone components. This results in bulk permeabilities very close to that of host rock (Shipton et al., 2002) to a factor of two lower than host rock (Antonellini and Aydin, 1994). However, as noted by several authors (Antonellini and Aydin, 1994; Shipton and Cowie, 2001), deformation bands form well-connected networks in 3D. Thus flow parallel to the fault zone must involve passing through deformation bands and the arithmetic average will overestimate permeability in this direction. The model results presented here suggest that permeability parallel to the major fault may be as much as one order of magnitude lower than host rock permeability. Since the harmonic average tends to underestimate permeability across the fault zone, and the arithmetic average overestimates bulk permeability parallel to the major fault, these methods can result in greatly overestimated permeability anisotropy.

From the model results, an analysis of the relative effects on bulk rock permeability of the fault damage zone (the focus of this paper) and the fault slip zone shows that the fault damage zone has a significant impact on the bulk permeability of the whole fault zone if the permeability of the slip zone fault rocks is similar to, or at the most one order of magnitude lower than, the permeability of deformation bands. The data from Shipton et al. (2002, Table 4) for a normal fault in porous sandstones can be used to compare the bulk permeability contributions of the damage zone and the slip zone, and the whole fault zone. In this case, the fault core permeability (1.4 mD) is higher than that of deformation bands (0.4 mD). Using their data on the number of deformation bands and the width of the damage zone allows the bulk permeability of the damage zone alone to be determined, from the harmonic average, as 70–120 mD. Taking the fault core alone into account gives permeabilities of 54–181 mD, showing that fault damage zone and fault core give approximately similar contributions to bulk permeability. Comparing these figures with their estimates for the whole fault zone of 35–72 mD shows a reduction in bulk permeability due to the addition of the fault core of much less than an order of magnitude. Since, in this case, the permeability ratio, R, of the fault core to the

deformation band is less than one, this is in agreement with the model results (Fig. 16).

In cases where the slip zone dominates the bulk permeability of the fault zone, the presence of the fault damage zone is still likely to have an important impact on the nature of two-phase flow and contaminant transport. It has been seen (Fig. 7) that the network of minor faults in the fault damage results in highly tortuous fluid pathways across the fault zone. In the absence of a damage zone, the effectiveness of the slip zone as a barrier to hydrocarbons or contaminants would be controlled by the places at which the thickness of fault rock is a minimum, places at which high pressure gradients would develop. The presence of the fault damage zone may shield these areas from such high pressure gradients by providing a further barrier to flow. In this way, the fault damage zone may be a major contributor to the containment properties of major faults, even when they provide only a minimal contribution to bulk fault zone permeability.

11. Conclusions

This numerical flow modelling study has shown how flow behaviour and bulk rock permeability vary with the spatial and orientation model type, the exponent of the power law length distribution, and the sub-region size. The main conclusions are as follows:

1. Of the three spatial and orientation models of fault damage zone architecture, model 3, which incorporates hierarchical clustering and faults oriented preferentially about the main fault, shows fault frequency profiles that most closely resemble natural fault damage zones.
2. Flow modelling through the 2D fault networks sub-sampled from the fault damage zone model show that preferential flow paths are developed for both flow perpendicular and parallel to the fault. Local flow magnitudes cover a wider range of three to four orders of magnitude.
3. The frequency distribution of bulk permeability is close to log–normal, with broader distributions (larger variances) for small sub-region sizes. Mean log permeability is constant with sample size. At the scale of the entire fault damage zone width (50 m), 99% of the permeability distribution spans an order of magnitude.
4. Mean log bulk permeability predicted by the models is between one and two orders of magnitude lower than the rock matrix permeability for flow perpendicular, and up to one and a half orders of magnitude lower for flow parallel, to the main fault.
5. Incorporating realistic orientation distributions (models 2 and 3) results in permeabilities more than half an order of magnitude different from the random model 1, resulting in anisotropies of around one order of magnitude. Incorporating spatial clustering (model 3) results in similar mean log bulk permeabilities but with higher variances.
6. A power law exponent of 1.8 results in bulk permeabilities half an order of magnitude lower perpendicular to, and half an order of magnitude higher parallel to the main fault, compared with an exponent of 2.2.
7. Fault damage zone efficiency as a flow barrier is defined relative to that of a region with one uniform-thickness spanning fault that contains the same proportion of fault rock. At a sub-region size of 50 m (spanning the damage zone), the damage zone is found to be 50% efficient perpendicular to, and between 1 and 10% efficient parallel to the main fault. The efficiencies of the fault networks are not sensitive to the power law length exponent.
8. The efficiency analysis provides a method of estimating bulk rock permeability from measurements of the proportion of fault rock in a damage zone based on outcrop and core. Analyses from damage zone data in the literature (Hesthammer et al., 2000; Shipton et al., 2002) are consistent with the model results.
9. The fault damage zone makes a significant contribution to the bulk fault zone permeability when the slip zone fault rock permeability is up to one order of magnitude lower than that of the minor faults. However, even when the fault slip zone dominates the bulk permeability of the whole fault zone, the fault damage zone is still likely to make a significant contribution to the fault sealing capacity.

Acknowledgements

The research presented in this paper was supported by the project ‘Scaling of fluid behaviour associated with flow through complex geological structures’ in the NERC Micro-to-Macro Thematic Program, and in part by EU funding through the Saltrans project (contract EVK1-CT-2000-00062).

References

Almeida, J.A., Soares, A., Pereira, M.J., Daltaban, T.S., 1996. Upscaling of permeability: implementation of a conditional approach to improve the performance in flow simulation. SPE 35490.

Antonellini, M., Aydin, A., 1994. Effect of faulting on fluid flow in porous sandstones: petrophysical properties. American Association of Petroleum Geologists Bulletin 78, 355–377.

Antonellini, M., Aydin, A., 1995. Effect of faulting on fluid flow in porous sandstones: geometry and spatial distribution. American Association of Petroleum Geologists Bulletin 79, 642–671.

Antonelli, M., Aydin, A., Orr, L., 1999. Outcrop-aided characterization of a faulted hydrocarbon reservoir: Arroyo Grande Oil Field, California, USA. In: W.C. Haneberg, P.S. Mozley, J.C. Moore, L.B. Goodwin (Eds.), Faults and Subsurface Flow in the Shallow Crust, AGU Geophysical Monograph 113, pp. 7–26.

Aydin, A., 2000. Fractures, faults and hydrocarbon entrapment, migration and flow. Marine and Petroleum Geology 17, 797–814.

Beach, A., Welbon, A.I., Brockbank, P.J., McCallum, J.E., 1999. Reservoir damage around faults: outcrop examples from the Suez rift. Petroleum Geoscience 5, 109–116.

Bonnet, E., Bour, O., Odling, N.E., Davy, P., Main, I., Cowie, P., Berkowitz, B., 2001. Scaling of fracture systems in geological media. Reviews of Geophysics 39, 347–383.

Caine, J.S., Forster, C.B., 1999. Fault zone architecture and fluid flow: insights from field data and numerical modelling. In: Haneberg, W.C., Mozley, P.S., Moore, J.C., Goodwin L.B. (Eds.), Faults and Subsurface Flow in the Shallow Crust. AGU Geophysical Monograph 113, pp. 101–127.

Caine, J.S., Evans, J.P., Forster, C.B., 1996. Fault zone architecture and permeability structure. Geology 24, 1025–1028.

Cardwell, W.T., Parsons, R.L., 1945. Average permeabilities of heterogeneous oil sands. Transactions of the American Institute of Mining, Metallurgical and Petroleum Engineers 160, 34–43.

Cheeney, R.F., 1983. Statistical Methods in Geology, George Allen and Unwin, London.

Chester, F.M., Logan, J.M., 1986. Implications for mechanical properties of brittle faults from observations of the Punchbowl fault zone, California. Pure and Applied Geophysics 124, 79–106.

Childs, C., Watterson, J., Walsh, J.J., 1995. Fault overlap zones within developing normal fault systems. Journal of the Geological Society of London 152, 535–549.

Cowie, P.A., Knipe, R.J., Main, I.G. (Eds.), 1996. Scaling laws for fault and fracture populations—analyses and applications. Journal of Structural Geology 18.

Evans, J.P., 1990. Thickness–displacement relationships for fault zones. Journal of Structural Geology 12, 1061–1065.

Fisher, Q.J., Knipe, R.J., 1998. Fault sealing processes in siliciclastic sediments. In: Jones, G., Fisher, Q.J., Knipe, R.J. (Eds.), Faulting, Fault Sealing and Fluid Flow in Hydrocarbon Reservoirs. Geological Society, London, Special Publications 147, pp. 117–134.

Fisher, Q.J., Knipe, R.J., 2001. The permeability of faults within siliclastic petroleum reservoirs of the North Sea and Norwegian continental shelf. Marine and Petroleum Geology 18, 1063–1081.

Flodin, E.A., Aydin, A., Durlofsky, L.J., Yeten, B., 2001. Representation of fault zone permeability in reservoir flow models. SPE 71617.

Fossen, H., Hesthammer, J., 1997. Geometric analysis and scaling relations of deformation bands in porous sandstone from the San Rafael desert, Utah. Journal of Structural Geology 19, 1479–1493.

Fowles, J., Burley, S., 1994. Textural and permeability characteristics of faulted, high porosity sandstones. Marine and Petroleum Geology 11, 608–623.

Foxford, K.A., Walsh, J.J., Watterson, J., Garden, I.R., Guscott, S.C., Burley, S.D., 1998. Structure and content of the Moab fault zone, Utah, USA, and its implications for fault seal prediction. In: Jones, G., Fisher, Q.J., Knipe, R.J. (Eds.), Faulting, Fault Sealing and Fluid Flow in Hydrocarbon Reservoirs. Geological Society, London, Special Publications 147, pp. 87–103.

Gabrielsen, R.H., 1990. Characteristics of joints and faults. In: Barton, N., Stephansson, O. (Eds.), Proceedings of the International Symposium on Rock Joints. International Society for Rock Mechanics, Loen, Norway, pp. 11–17.

Gillespie, P.A., Walsh, J.J., Watterson, J., 1992. Limitations of dimension and displacement data from single faults and the consequences for data analysis and interpretation. Journal of Structural Geology 14, 1157–1172.

Harris, S.D., McAllister, E., Knipe, R.J., Elliott, L., Ingham, D.B., 1999. Scaling of fluid flow associated with flow through fault damage zones and networks. In: Lippard, S.J., Naess, A., Sinding-Larsen, R. (Eds.), Proceedings of the 5th Annual Conference of the International Association for Mathematical Geology. Tapir, Trondheim, pp. 711–716.

Harris, S.D., McAllister, E., Knipe, R.J., Odling, N.E., 2003. Predicting the three-dimensional population characteristics of fault damage zones: a study using stochastic models. Journal of Structural Geology 25, 1281–1299.

Hesthammer, J., Johansen, T.E.S., Watts, L., 2000. Spatial relationships within fault damage zones in sandstone. Marine and Petroleum Geology 17, 873–893.

Jourde, H., Flodin, E.A., Aydin, A., Durlofsky, L.J., Wen, X.-H., 2002. Computing permeability of fault zones in eolian sandstones from outcrop measurements. American Association of Petroleum Geologists Bulletin 86, 1187–1200.

Knipe, R.J., Fisher, Q.J., Jones, G., Clennell, M.B., Farmer, A.B., Harrison, A., Kidd, B., McAllister, E., Porter, J.R., White, E.A., 1997. Fault seal analysis: successful methodologies, application and future directions. In: Møller-Pedersen, P., Koestler, A.G. (Eds.), Hydrocarbon Seals: Importance for Exploration and Production. Norwegian Petroleum Society (NPF) Special Publication 7, pp. 15–40.

Knipe, R.J., Jones, G., Fisher, Q.J., 1998. Faulting, fault seal and fluid flow in hydrocarbon reservoirs: an introduction. In: Jones, G., Fisher, Q.J., Knipe, R.J. (Eds.), Faulting, Fault Sealing and Fluid Flow in Hydrocarbon Reservoirs. Geological Society, London, Special Publications 147, pp. vii–xxi.

Knott, S.D., Beach, A., Brockbank, P.J., Lawson Brown, J., McCallum, J.E., Welbon, A.I., 1996. Spatial and mechanical controls on normal fault populations. Journal of Structural Geology 18, 359–372.

Kumar, A., Farmer, C.L., Jerauld, G.R., Li, D., 1997. Efficient upscaling from cores to simulation models. SPE 38744.

McGrath, A.G., Davidson, I., 1995. Damage zone geometry around fault tips. Journal of Structural Geology 17, 1011–1024.

Manzocchi, T., Walsh, J.J., Nell, P., Yielding, G., 1999. Fault transmissibility multipliers for flow simulations models. Petroleum Geoscience 5, 53–63.

Matheron, G., 1967. Elements Pour une Theorie des Milleux Poreux, Maison et Cie, Paris.

Muskat, M., 1937. Flow of Homogeneous Fluids, McGraw-Hill, New York.

Nicol, A., Watterson, J., Walsh, J.J., Childs, C., 1996. The shapes, major axis orientations and displacement patterns of fault surfaces. Journal of Structural Geology 18, 235–248.

Odling, N.E., Webman, I., 1991. A conductance mesh approach to the permeability of natural and simulated fracture pattern. Water Resources Research 27, 2633–2643.

Pickup, G.E., Ringrose, P.S., Corbett, P.W.M., Jensen, J.L., Sorbie, K.S., 1995. Geology, geometry and effective flow. Petroleum Geosciences 1, 37–42.

Press, W.H., Teukolsky, S.A., Vetterling, W.T., Flannery, B.P., 1992. Numerical Recipes, 2nd Ed, Cambridge University Press.

Renard, P., de Marsily, G., 1997. Calculating equivalent permeability: a review. Advances in Water Research 20, 253–278.

Rippon, J.H., 1985. Contoured patterns of the throw and hade of normal faults in the coal measures (Westphalian) of north-east Derbyshire. Proceedings of the Yorkshire Geological Society 45, 147–161.

Sanchez-Vila, X., Girardi, J.P., Carrera, J., 1995. A synthesis of approaches to upscaling of hydraulic conductivities. Water Resources Research 31, 867–882.

Shipton, Z.K., Cowie, P.A., 2001. Damage zone and slip-surface evolution over μm to km scales in high-porosity Navajo sandstone, Utah. Journal of Structural Geology 23, 1825–1844.

Shipton, Z.K., Evans, J.P., Robeson, K.R., Forster, C.B., Snelgrove, S., 2002. Structural heterogeneity and permeability in faulted eolian sandstone: implications for subsurface modelling of faults. American Association of Petroleum Geologists Bulletin 86, 863–883.

Sibson, R.H., 1992. Implications of fault valve behaviour for rupture nucleation and recurrence. Tectonophysics 211, 283–293.

Wealthall, G.P., Steele, A., Bloomfield, J.P., Moss, R.M., Lerner, D.N., 2001. Sediment filled fractures in the Permo-Triassic sandstones of the Cheshire Basin: observations and implications for pollutant transport. Journal of Contaminant Transport, 50, 41–51.